Long-term slip rates and fault interactions under low contractional strain, Wanganui Basin, New Zealand

Geoffroy Lamarche, Jean-Noël Proust, Scott D. Nodder

Long-term slip rates and fault interactions under low contractional strain, Wanganui Basin, New Zealand

Geoffroy Lamarche

National Institute of Water and Atmospheric Research, Wellington, New Zealand

Jean-Noël Proust

Géosciences Rennes, Université de Rennes 1, Rennes, France

Scott D. Nodder

National Institute of Water and Atmospheric Research, Wellington, New Zealand

Received 10 June 2004; revised 16 January 2005; accepted 29 March 2005; published 15 July 2005.

[1] The newly mapped Kapiti-Manawatu Fault System (KMFS) in southern North Island, New Zealand, accommodated ~3.5 km of basement throw over the last 3 Myr. Along-strike throw profiles are generated using seven stratigraphic markers, interpreted from seismic reflection profiles acquired <3 km apart. The profiles are symmetrical about their point of maximum displacement, and cumulative profiles suggest that the reverse fault system behaves coherently. The KMFS originates from the reactivation of extensional structures, with fault lengths remaining constant over time. Contractional deformation started at circa 1750 ± 400 ka. Maximum dip-slip rates along individual faults are 1.77 ± 0.53 and 0.74 ± 0.22 mm yr^{-1} for the 0–120 and 120–1350 ka periods, respectively. The maximum cumulative throw rates across the KMFS are 4.9 ± 1.5 and 1.5 ± 0.5 mm yr^{-1} for the same periods. Long-term strain rates across the KMFS are 2–5 times smaller than strain rates in the forearc basin of the Hikurangi subduction margin located less than 100 km to the east. The faults of the KMFS may extend to depth and link with the subducted Pacific plate. **Citation:** Lamarche, G., J.-N. Proust, and S. D. Nodder (2005), Long-term slip rates and fault interactions under low contractional strain, Wanganui Basin, New Zealand, *Tectonics*, *24*, TC4004, doi:10.1029/2004TC001699.

1. Introduction

[2] Fault length and throw are key parameters in characterizing structural styles and are requirements for fault population analysis [*Childs et al.*, 2003; *Cowie and Scholz*, 1992; *Walsh et al.*, 2002] and hazard modeling [e.g., *Stirling et al.*, 2000]. Quantitative analysis of displacements in normal fault arrays have led to the development of the "isolated" and "coherent" fault growth models [*Mansfield and Cartwright*, 1996; *Walsh et al.*, 2003] (Figure 1). In the isolated fault model, individual fault segments are kinematically independent, and fault relays are incidental. On the other hand, in the coherent fault model individual faults and fault relays are kinematically dependent and fault segments are connected by ductile strain, or distributed deformation, in the rock volume. In the coherent fault model, while discrete faults concentrate macroscopic deformation, ductile strain and plastic deformation contribute largely to the total strain accommodated in the deformed region of the upper crust [e.g., *Walsh et al.*, 1996].

[3] Neither of these models have been properly established or applied to reverse fault systems. This may be because time horizons in uplifted hanging walls of reverse faults are often not deposited or are eroded, hence preventing detailed temporal analysis of fault activity. Locally, however, deformed strata may be preserved on the flanks of sedimentary basins, enabling strain evolution across the deformation zone to be quantified. This is the case for convergent margins where strain across subduction systems extends over hundreds of kilometers behind the subduction front, varying spatially in structural style and through time.

[4] The southern Wanganui Basin (SWB), North Island, New Zealand, is located approximately 200 km landward of the Hikurangi subduction margin (Figure 2). Plio-Pleistocene contractional deformation along the eastern edge of the basin, together with more than 4 km of basin subsidence, relate to high degree of coupling along the 30- to 40-km-deep subducted Pacific-Australia (Pac-Aus) plate interface [*Stern et al.*, 1992]. Subsidence of the SWB is controlled by a predominantly reverse fault system along its eastern flank, newly named here the Kapiti Manawatu Fault System (KMFS). The KMFS is characterized by good preservation of dated sedimentary horizons in both the hanging walls and footwalls of many of the faults. This provides a rarely observed framework where we can investigate the temporal and spatial evolution of a reverse fault system and evaluate the implications of this development to the progressive evolution of the Hikurangi subduction system over the last 2–3 Myr.

[5] This paper presents in detail the spatial and temporal evolution of the KMFS using seven key chronostratigraphic

0278-7407/05/2004TC001699

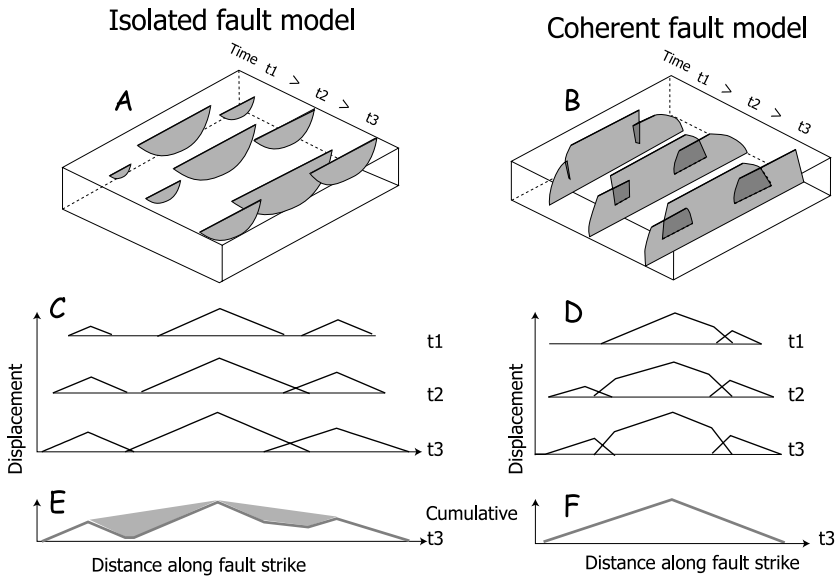

Figure 1. Temporal evolution of (a) an isolated fault system and (b) a coherent fault system. (c–f) Schematic diagrams showing the evolution in time (t1 > t2 > t3) of an isolated (Figure 1a) and a coherent (Figure 1b) fault system with their relative distances along strike-displacement profiles (Figures 1c and 1d), and relative cumulative (aggregate) displacement profiles at t3 (Figures 1e and 1f). In the isolated fault model, the cumulative displacement profile shows deficits in displacement between the adjacent fault segments (shaded areas), with the points of maximum displacement being preserved. In contrast, the cumulative displacement profiles for the coherent fault model (Figure 1f) has a simple triangular shape, with no displacement deficit. Modified from *Walsh et al.* [2003] with permission.

markers defined within the Plio-Pleistocene (<3 Myr) sedimentary sequence that infill the SWB. The study is based on the interpretation of a large data set of multichannel seismic (MCS) reflection profiles first published here, providing excellent constraints on the geometry of the fault system. The detailed analysis of the sedimentary architecture and evolution of the basin through time is provided in a companion paper [*Proust et al.*, 2005], while the quantification of short-term slip rates and earthquake recurrence intervals from analysis of surface fault scarps will be provided elsewhere (S. D. Nodder et al., manuscript in preparation, 2005). The aim of this paper is twofold: (1) to investigate fault interactions in the KMFS so as to demonstrate that fault populations in contractional settings may form coherent fault systems; and (2) to quantify the evolution of the deformation during the last 3 Myr along the western edge of the Pacific-Australia plate boundary deformation zone in southern North Island, New Zealand, in order to constrain contractional strain rates across the upper plate in the geodynamic context of a highly coupled plate interface.

2. Neogene Structural and Tectonic Patterns

[6] The structural style in the SWB represents the westernmost expression of Neogene contractional deformation in the upper plate of the southern Hikurangi subduction margin. Subduction along the margin was initiated circa 25 Ma [e.g., *Kamp*, 1986; *Walcott*, 1984]. The SWB lies north of the intracontinental transpression zone generated along the Alpine Fault, and south of the Taupo Volcanic Zone (TVZ), a continental, extensional back-arc basin with active volcanism and pervasive normal faulting [e.g., *Stern and Davey*, 1989] (Figures 2 and 3). In contrast to the >4 km of Plio-Pleistocene subsidence that has occurred in the offshore SWB [*Anderton*, 1981], the northern onshore part of the basin has undergone 2–3 km of uplift and erosion since the late Miocene [*Pillans*, 1986].

2.1. Southern North Island

[7] Between 40°S and 41°S, the present-day Pacific-Australia relative plate motion vector is 40–42 mm yr^{-1} with an azimuth of N261°E [*DeMets et al.*, 1994] (Figure 2). Partitioning of deformation in the overlying Australian Plate has resulted in a well-developed, late Cenozoic, imbricated accretionary prism, east of the North Island [*Collot et al.*, 1996; *Lewis and Pettinga*, 1993], and a late Miocene to mid-Quaternary forearc basin in southeastern North Island [e.g., *Beanland*, 1995; *Beanland et al.*, 1998]. At the latitude of the SWB, only 14 mm yr^{-1} of relative plate motion is accommodated between the east and west coasts of southern North Island, accounting for <30% of the total predicted plate convergence [*Barnes et al.*, 1998; *Darby and Beavan*, 2001; *Nicol and Beavan*, 2003]. In addition, *Barnes et al.* [2002] suggest that only 8–20% of the plate convergence is accommodated between the east coast of the North Island and the Hikurangi subduction front at ~39.5°S. These studies suggest that further constraints on

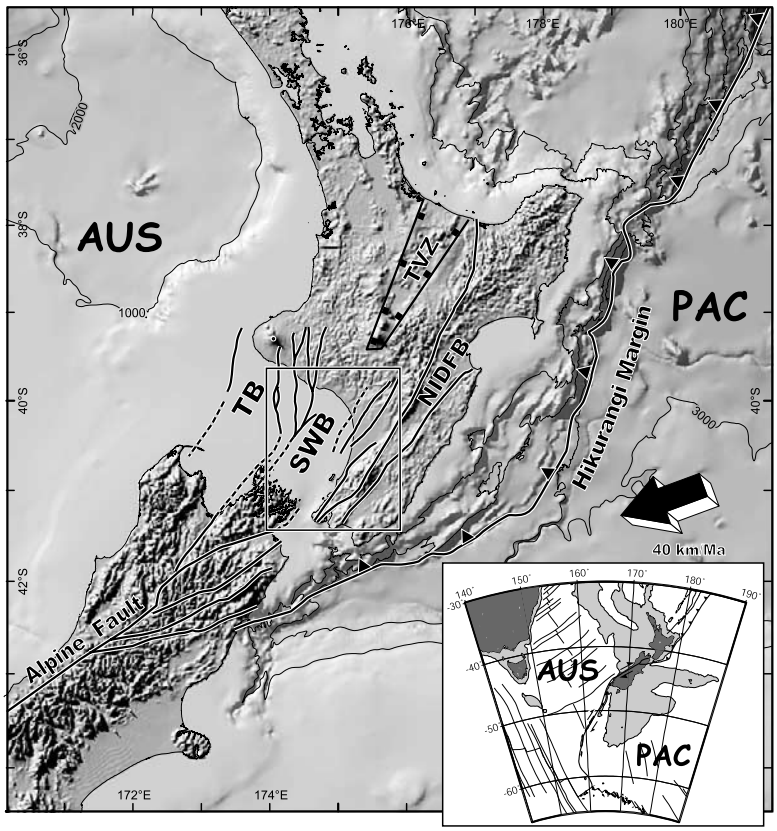

Figure 2. Location of the study area in the New Zealand geodynamic environment. Toothed line indicates the Hikurangi subduction front. The large black arrow indicates the Pacific Plate (PAC) motion relative to the Australian Plate (AUS) [*DeMets et al.*, 1994]. Note that the relative plate vector is ~50° oblique to the Hikurangi subduction margin north of ~41°S and becomes subparallel to the plate boundary southward. Bold lines indicate major geological faults. SWB, southern Wanganui Basin; NIDFB, North Island Dextral Fault Belt; TB, Taranaki Basin; The intense normal faulting activity occurring in the back-arc region of the Taupo Volcanic Zone (TVZ) is indicated with thick dash lines. Insert shows the location of the New Zealand continent within the South Pacific region. Thick line shows the Pacific-Australia plate boundary; thin lines show the fracture zones. Gray shading indicates water depths less than 2000 m.

the regional strain distribution across the southern North Island are required to estimate the total partitioning of deformation within the upper plate.

[8] Deformation in the upper plate, at the latitude of the SWB, is partitioned between strike-slip deformation, essentially along the North Island Dextral Fault Belt (NIDFB, Figure 2) [*Beanland*, 1995], and compressive deformation in the forearc basin and along the eastern margin of the SWB. Contraction across the plate boundary zone has facilitated the progressive uplift of the 1100-m-high North Island Axial Ranges over the last 1–2 Myr [*Ghani*, 1978; *Lamb and Vella*, 1987]. To the west of the Axial Ranges, a series of active strike-slip faults run subparallel to the west coast of the lower North Island (Figure 3). Although on land the surface expressions of these faults are poor, they extend northward from the Wellington Peninsula and possibly offshore along the eastern margin of the SWB. Horizontal slip rates of 0.8–1.4 mm yr^{-1} are estimated for the Shepherds Gully and Pukerua faults and 1–3 mm yr^{-1} for the northern Ohariu Fault over the last 18 kyr [*Van Dissen and Berryman*, 1996] (Figure 3). There are no vertical slip rate measurements available for these faults.

[9] Most evidence of faulting beneath the coastal floodplain between the axial ranges and the coast are masked, but interpretation of scarce MCS profiles provides the general location of the Turakina, Rangitikei, and Rauoterangi faults [*Anderton*, 1981] (Figure 3). Average dip-slip rates estimated on reverse faults along the west toe of the Axial Ranges range 0.1–0.5 mm yr^{-1} [*Aharoni*, 1991; *Jackson et al.*, 1998; *Melhuish et al.*, 1996]. Between 40°45′S and 40°30′S, beneath the floodplain, a series of half grabens are bounded by normal faults with vertical offsets of up to 500 m [*Aharoni*, 1991].

2.2. Southern Wanganui Basin

[10] The SWB has an elongated NNE-SSW trend and is located between two elevated Paleozoic-Mesozoic basement

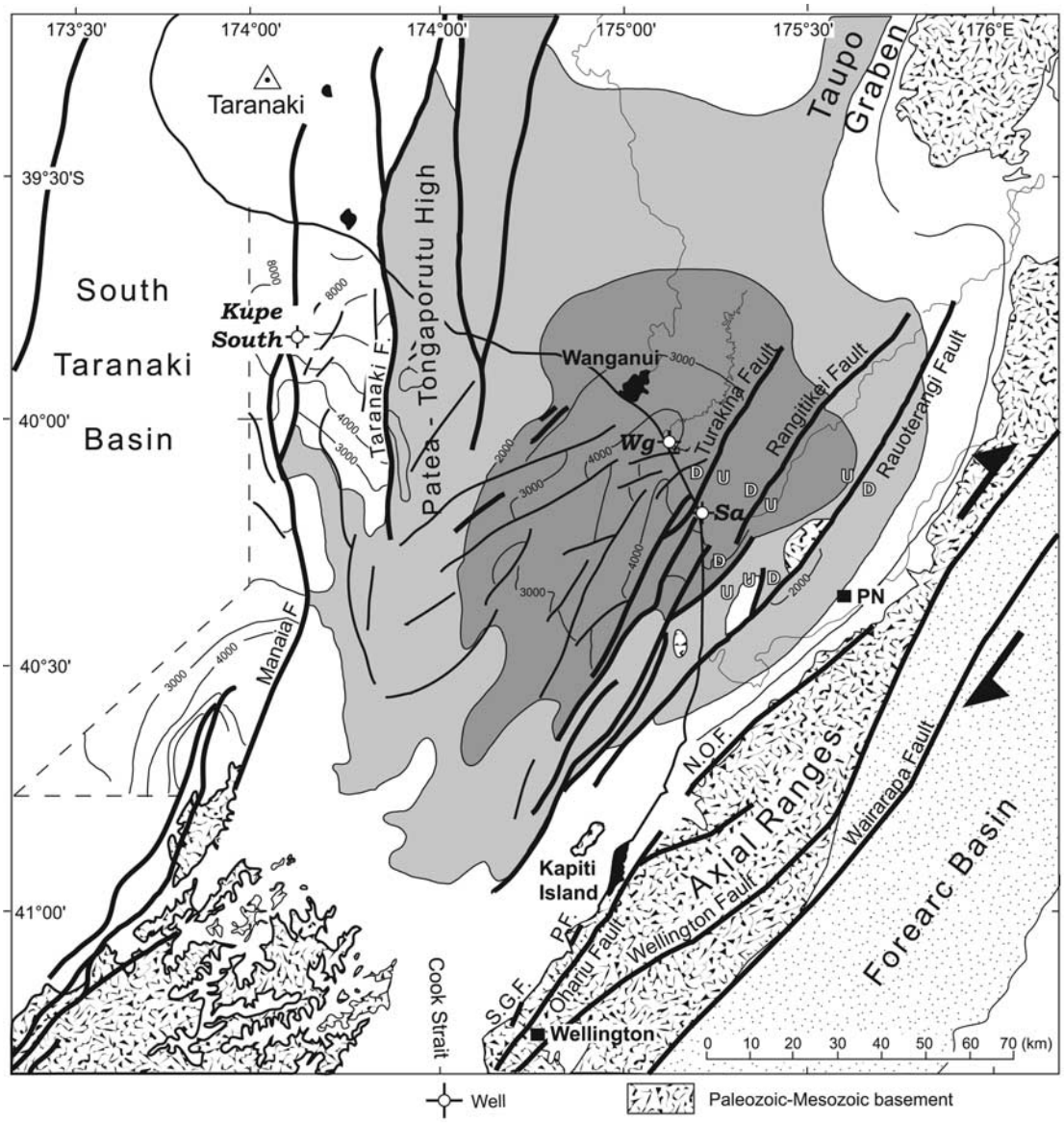

Figure 3. Structural setting of the southern Wanganui Basin (SWB), modified after *Anderton* [1981], with permission from the Royal Society of New Zealand (http://www.rsnz.org/publish/nzjgg). Thin contour lines indicate the depth to graywacke basement in meters below mean sea level, with gray shading enhancing the 1000 and 2000 m depths. Basement faults are indicated, with the main faults in bold. U/D indicates the up/down side of fault, irrespective of the sense of displacement. The Wellington and Wairarapa faults are part of the North Island Dextral Fault Belt (NIDFB, see text and Figure 2). P.F., Pukerua Fault; S.G.F., Shepherd Gully Fault; N.O.F., Northern Ohariu Fault. Coastal and offshore oil exploration wells are indicated: Sa, Santoft; Wg, Whangaehu. PN, Palmerston North city.

blocks, the submerged Patea-Tongaporutu High to the west and the emergent, recently uplifted (<2 Ma) North Island Axial Ranges to the east [*Katz and Leask*, 1990; *Wilson and McGuire*, 1995] (Figure 3). Early interpretations of several high-angle reverse faults located along the eastern border of the SWB attributed their origin to dextral wrench deformation [*Anderton*, 1981; *Thompson et al.*, 1994]. Lithospheric-scale models and recent onshore studies, however, suggest that wrench deformation is not significant in the SWB [*Melhuish et al.*, 1996; *Stern et al.*, 1992]. *Stern et al.* [1992, 1993] propose that the major reverse structures on the eastern margin of the SWB and the normal faults on its western border originate from broad-scale lithospheric flexure related to high frictional coupling at the plate interface, superimposed on subsidence driven by sediment loading. The strong negative gravity field (−150 mGal anomaly) [*Hunt*, 1980] and an unusually deep Moho (>40 km) [*Stern and Davey*, 1989] associated with the SWB are also

Table 1. Ages and Interval Velocities Used for Depth Conversion of Seven Key Stratigraphic Markers and Acoustic Basement in the KMFS[a]

Horizon	Age, ka	Interval Velocity, m s^{-1}
H1	120 ± 20	1630 ± 100
H2	620 ± 20	1870 ± 180
H3	1000 ± 20	2160 ± 320
H4	1350 ± 40	2560 ± 520
H5	2400 ± 40	3000 ± 640
H6	2600 ± 40	3000 ± 640
H7	3000 ± 50	3000 ± 640
Average		2300 ± 460

[a]Constraints on horizon ages are provided by *Proust et al.* [2005]. Interval velocities for horizons H1 to H5 are calculated from smoothed stacking velocity models generated along seismic profiles. Conversion from stacking to interval velocities is performed using the Dix equation. We ignore velocities derived from the CR3048 survey as too unreliable. NMO-derived interval velocities for horizons H6 to H7 are 30–40% higher than that measured from sonic logs in Santoft-1 and Kupe South-5 wells and were capped at 3000 m s^{-1}. Average is weighted average velocity calculated for the entire sedimentary sequence in the thickest part of the basin and used for calculating throws of the basement reflector.

consistent with widespread crustal shortening and lithospheric-scale downwarping.

[11] Composite fault plane solutions for small, shallow earthquakes ($M_L > 3.5$, depth <12 km) over the 1964–1980 period in the SWB indicate normal focal mechanisms with horizontal tension axes oriented nearly east-west [*Garrick and Gibowicz*, 1983]. Focal mechanisms for large earthquakes indicate reverse faulting with a component of strike-slip with the top of the subducted Pacific Plate estimated to be at depths of 30–40 km in the SWB [*Robinson*, 1986; *Stern and Davey*, 1989].

3. Sedimentary Environment

[12] The majority of the 4- to 5-km-thick sedimentary sequence in the SWB accumulated during the Pliocene and Pleistocene and lie unconformably on highly irregular and deformed Permian-Jurassic metamorphic basement rocks that crop out in the axial ranges and northern South Island (Figure 3). The SWB basin has developed essentially by progressive subsidence and sedimentary onlap to the southeast, concurrent with emergence and offlap to the north, resulting in the southeastward migration of the main epicenter through time [*Anderton*, 1981; *Kamp and Turner*, 1990]. During basin development, the two structural highs bounding the basin (namely, the Patea-Tongaporutu High and the axial ranges) channelized sediment transport and deposition in a southeastward direction [*Proust et al.*, 2005].

[13] Detailed seismic facies of the Plio-Pleistocene sedimentary basin fill in the SWB are examined in detail in a companion paper [*Proust et al.*, 2005] which provides the basis of the time constraints on fault activity in the KMFS. Seven prominent seismic reflectors (H1 to H7, Table 1), which represent basin-wide unconformities, were correlated throughout the seismic grid, along with an additional two reflectors (H8 to H9) that only occur in the western part of the basin. Ages and lithologic control on the seismic stratigraphy (Table 1) are provided by correlations with data from oil exploration drill holes, onshore coastal geological cross sections [e.g., *Carter and Naish*, 1998; *Fleming*, 1953; *Naish et al.*, 1999] and synthetic seismograms generated using wire line logs recorded in the Kupe-South and Santoft wells (location on Figures 3 and 4 [*Proust et al.*, 2005]). The synthetic seismograms were correlated to composite lithostratigraphic columns from *Kamp et al.* [2002]. The uppermost horizon H1 is best correlated to an unconformity related to the Rapanui Terrace formation at circa 120 ka [*Pillans*, 1991], although possible correlation to the Waipuna Conglomerate unconformity provide an alternative age of ~260 ka [*Naish et al.*, 1999]. The H4 horizon is correlated to the regional uncomformity recognized onshore at the base of the Castlecliff-type section [*Fleming*, 1953] and is dated at the base of the New Zealand Castlecliffian stage (1350 ± 40 ka).

4. Data and Method

4.1. Seismic Reflection Data

[14] We interpreted a large network of MCS reflection profiles (Figure 4) acquired for research and industry purposes. This data set results in a maximum line spacing of 3 km and an average of 1.5 km over the study area. The bulk of the MCS data used in this study were acquired by the National Institute of Water and Atmospheric Research (NIWA) Ltd. (survey CR3048, November 1998, and TAN0105, May 2001) and are first published here. NIWA MCS data have a maximum apparent frequency of 150 Hz and excellent resolution down to 1.5 s two-way travel time (abbreviated as s throughout the paper). The trace spacing of 3–6 m results in good lateral resolution on all NIWA seismic profiles.

[15] Oil industry MCS data collected during the 1970s [*Anderton*, 1981] were reprocessed in the early 1990s [*Katz and Leask*, 1990; *Thompson et al.*, 1994] and are characterized by low apparent frequencies (5–30 Hz), which result in lower resolution for many sedimentary features. The data provide good imaging of, and beneath the basement reflector down to 5 s. The substantially longer seismic streamers (2100–2350 m) used during acquisition of industry data, compared with that of NIWA (300 m for CR3048 and 600 m for TAN0105), provide better constraints on the seismic velocities derived from stacking velocities. In general, industry seismic reflection data display reduced seafloor multiples and reverberated energy, compared to the NIWA data set.

[16] Processing applied to the NIWA data set includes true amplitude recovery, custom-designed band-pass filter and predictive deconvolution functions. The very shallow water depths (20–150 m) in the coastal zone are sometimes accompanied by hard seafloor substrates, which result in very high amplitude and pervasive first-order seafloor multiples as well as reverberated (peg legs) energy. Extensive tests to attenuate the multiples were only moderately successful for the CR3048 data, mainly due to the short

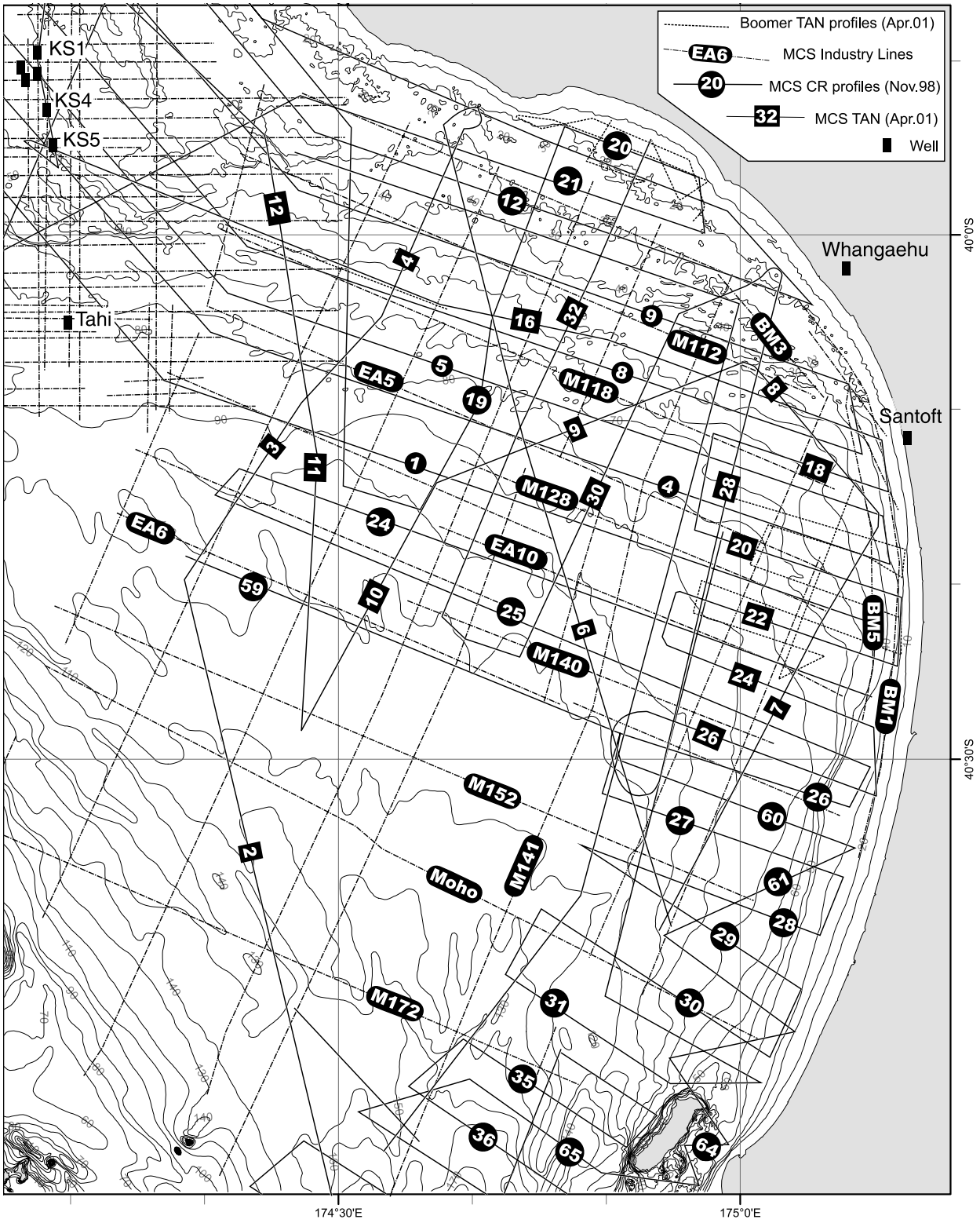

Figure 4. Marine multichannel seismic (MCS) reflection profiles in the SWB. The data set consists of MCS profiles acquired by the oil industry (alternate dashed line) and during the two research surveys CR3048 (Nov-98, abbreviated to CR) and TAN0105 (May-01, abbreviated to TAN). High-resolution (3.5 kHz) seismic reflection data were collected along all research MCS profiles and very high resolution seismic Boomer data (dashed line) were collected in the coastal zone.

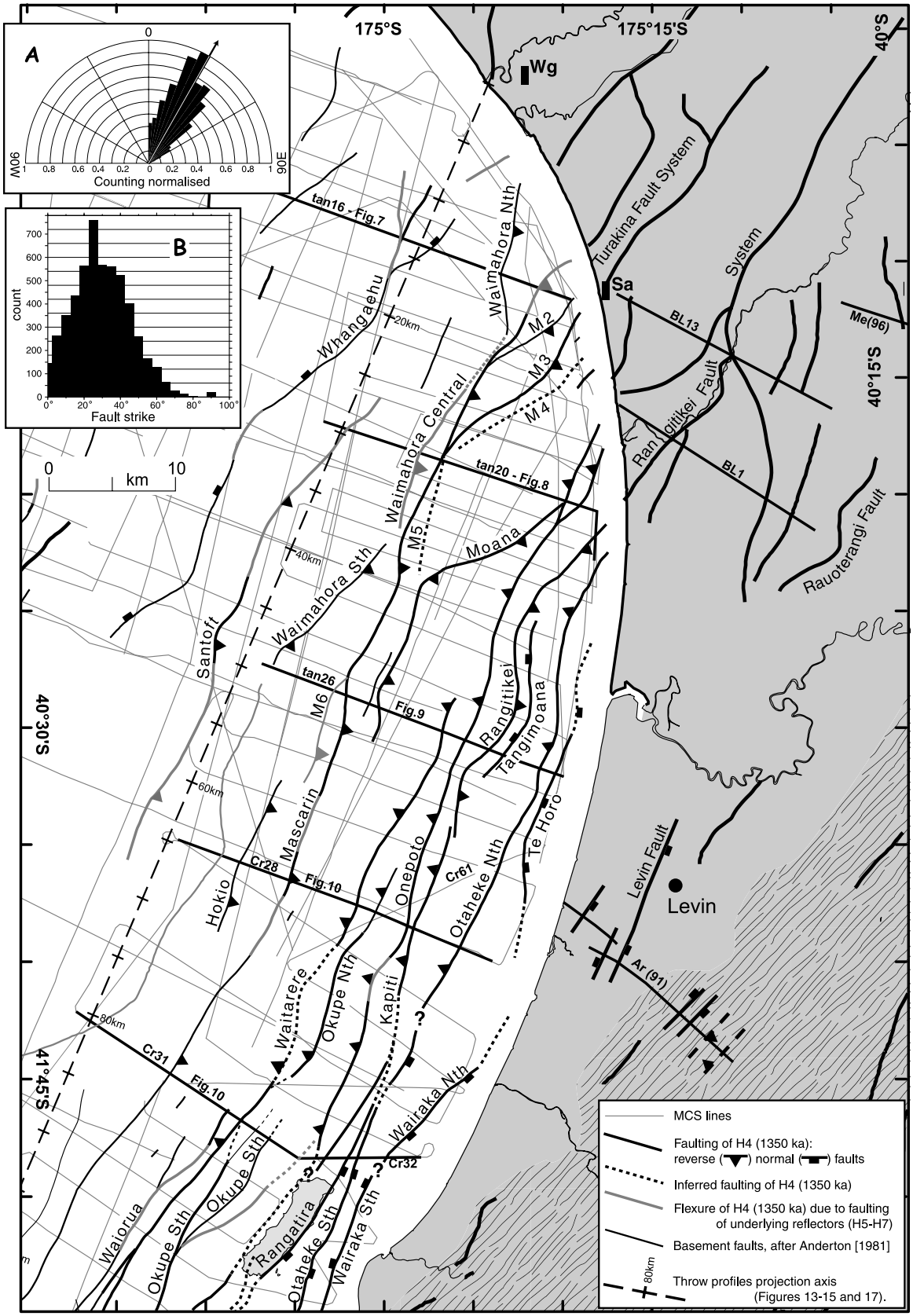
A
Counting normalised
B
count
Fault strike
0 km 10
175°S
175°15'S
40°S
40°15'S
40°30'S
41°45'S
Wg
Sa
Levin
Turakina Fault System
Ran gitikei Fault
Rauoterangi Fault
Levin Fault
Waimahora Nth
Whangaehu
Waimahora Central
Waimahora Sth
Santoft
Moana
Rangitikei
Tangimoana
Mascarin
Hokio
Onepoto
Otaheke Nth
Te Horo
Waitarere
Okupe Nth
Kapiti
Waitaka Nth
Okupe Sth
Otaheke Sth
Waiorua
Rangatira
Wairaka Sth
M2
M3
M4
M5
M6
tan16 - Fig.7
tan20 - Fig.8
tan26
Fig.9
Fig.10
Cr28
Cr67
Cr31
Cr32
BL13
BL1
Me(96)
Ar(91)
20km
40km
60km
80km
MCS lines
Faulting of H4 (1350 ka): reverse (▼) normal (▬) faults
Inferred faulting of H4 (1350 ka)
Flexure of H4 (1350 ka) due to faulting of underlying reflectors (H5-H7)
Basement faults, after Anderton [1981]
Throw profiles projection axis (Figures 13-15 and 17).

Figure 5

streamer that trawled at irregular depths. Acquisition and multiple attenuation were improved significantly for the TAN0105 profiles when depth controllers were used on the streamer. Interactive muting of long offsets was required in many places due to the intense refracted signal caused by the shallow water depths.

4.2. Throw Measurements and Throw Rate Estimates

[17] Fault throws, or vertical separations, estimated from key stratigraphic markers offsets are converted from measurements in time to displacements in meters using a velocity model generated from MCS data tuned to well wire line logs and synthetic seismic logs (Table 1). The depth-converted profiles are also used to estimate fault dips. Along strike-projected throw profiles for the key stratigraphic markers are generated along all faults. Throw profiles are widely used to display the evolution of fault displacements and to provide information on fault interactions across extensional fault systems [e.g., *Childs et al.*, 1993]. The N23°E projection axis corresponds to the trend of the KMFS, and the axis origin (at 0 km) is located at the coastline to the north of the study area (Figure 5). Profiles of throw versus time are used to derive rates for individual faults. In cases where faults are too closely spaced to attribute displacement to individual structures, the horizon offset is measured across all related faults and attributed to the largest structure (e.g., Mascarin Fault and associated splays).

4.3. Errors

[18] Large errors are associated with throw measurements on MCS profiles, and therefore on the derived rates. The sources of error on fault offsets arise essentially from uncertainties in horizon picks and in the interval velocities used for depth conversions (Table 1). Errors on the velocities used for depth conversions are given by the standard deviation derived from the interval velocity means (Table 1) and range from 5% at shallow depths to 20% below H4. Uncertainties in horizon interpretation originate largely from data resolution and quality and therefore increase with depth. The correlation of horizons throughout the MCS network (Figure 4), however, minimizes the relative error on horizon depths. Arbitrarily, we estimated the minimum relative error on horizon picking to a maximum of two wavelengths at shallow depths (<500 ms) and four wavelengths below 500 ms. The maximum frequency at shallow depths is ~140 Hz, reducing to ~100 Hz at 1 s and 70 Hz at 1.5 s, yielding a ~15 ms error at the seafloor, increasing to 20 ms at 1 s and 50 ms at 1.5 s.

[19] The largest uncertainties on throw measurements are related to fault drag occurring adjacent to the fault plane in both the footwall and the hanging wall. The localized bending of reflectors associated with faulting effectively minimizes the throw between reflector cutoffs and is accounted for by extending the trend of undeformed parts of the reflectors, linearly toward the fault plane on both the footwall and hanging wall [*Chapman and Meneilly*, 1991]. The resulting minimum errors on throws are 10% for the upper horizons (H1 to H3), 15% for H4 and H6 and 20% for the basement horizon.

[20] The errors on slip rates equate to the sum of the errors on horizon ages and throws. A 15% error on horizon ages is estimated from errors inherent in the lithostratigraphical and chronostratigraphical correlations between well logs and coastal geological sections [*Proust et al.*, 2005]. The minimum error on throw rates is estimated to be ~30% unless otherwise stated. Other sources of uncertainty, for example, those associated with data acquisition and time migration, are considered negligible (for a review of errors in MCS interpretation, see *Thore et al.* [2002]).

5. Structural Patterns in the Kapiti-Manawatu Fault System

[21] The structural map presented here is based on the faulting of the H4 (1350 ± 40 ka) horizon (Figure 5). The map shows a well-constrained 20- to 25-km-wide fault zone, with a very consistent average N20°–30°E fault trend (Figure 5, insets). Eighteen individual faults are identified in the KMFS (Table 2), with good correlation between seismic lines where the line spacing is less than ~1.5 km. Reverse faults are widespread across the fault system and normal faults are observed in the southeastern edge of the KMFS.

[22] The regional basement structure along the KMFS (Figure 6) is that of an asymmetric, highly discordant, basement high, with a steep eastern flank and gently dipping western flank. The basement high, easily identified on all MCS lines, crops out at Kapiti Island and plunges northward to form a well-defined, N15°E trending ridge.

[23] In the following, we provide descriptive and quantitative information on the faults of the KMFS, using a series of MCS profiles (Figures 7 to 10) perpendicular to the fault trend.

5.1. West KMFS: Mascarin, Waimahora, and Hokio Faults

[24] The Mascarin, Waimahora, and Hokio faults (new names) are east dipping reverse faults, which mark the westernmost expression of the KMFS and the boundary between the Kapiti basement high to the east and the deep SWB basin floor to west. The Mascarin Fault displays the

Figure 5. Faulting of H4 (1350 ka) key stratigraphic marker along the Kapiti Manawatu Fault System (KMFS). Onshore MCS profiles used to correlate offshore faults with that of the present study are indicated as follows: Me(96), *Melhuish et al.* [1996]; Ar(91), *Aharoni* [1991]; BL1 and BL13, industry profiles [*Anderton*, 1981]. The striped pattern in the lower right corner represents graywacke basement of the Axial Ranges. Onshore wells at Whangaehu (Wh) and Santoft (Sa) are also shown. Onshore faults are courtesy of the Institute of Geological and Nuclear Sciences (GNS) Ltd., Lower Hutt, New Zealand. Inset A is a fault rose diagram and inset B is fault histogram; these are computed after decimation of each fault into ~170-m-long segments (5269 segments in total). This prevents biasing the diagrams toward the longest faults in the KMFS.

Table 2. Maximum Values of Throw, Throw Rate, and Length of Individual Faults in the KMFS[a]

Fault	R/N	L.H1 (Line)	Th.H1	TR.H1	L.H4 (Line)	Th.H4	TR.H4	Th.H4-H1	TR.H4-H1	Th.Bas	L1	L2	L3
Hokio	R	63 (m152)	90	0.75 ± 0.23	63 (m152)	240 ± 30	0.18 ± 0.05	150	0.12 ± 0.04	240 ± 30	15	5	-
Kapiti	R	72 (cr62)	80	0.67 ± 0.2	72 (cr62)	313[b] ± 63	0.23 ± 0.07	233	0.19 ± 0.06	430 ± 60	42	31	-
Mascarin	R	38.5 (cr24)	200	1.67 ± 0.5	17 (tan8)	1050 ± 210	0.78 ± 0.23	850	0.69 ± 0.21	1380 ± 200	66[c]	42	92-102
Mascarin 2[d]	R										8		
Mascarin 3[d]	R										14		
Mascarin 4[d]	R										13[c]		
Mascarin 5[d]	R										10		
Moana	R	39 (cr24)	73	0.61 ± 0.18	45 (cr25)	400 ± 80	0.30 ± 0.09	327	0.27 ± 0.08	550 ± 80	28	12,13	-
Okupe	R	71 (cr62)	60	0.50 ± 0.15	71 (cr62)	270 ± 54	0.20 ± 0.06	210	0.17 ± 0.05	270 ± 60	40	15	Sth
Onepoto	R	34.5 (tan22)	150	1.25 ± 0.38	22 (bm1)	590 ± 110	0.44 ± 0.13	440	0.36 ± 0.11	690 ± 220	78[c]	45	90
Otaheke-Nth	R	56 (cr61)	100	0.83 ± 0.25	56 (cr61)	570[b] ± 100	0.42 ± 0.13	470	0.38 ± 0.11	770 ± 460	38[c]	32	50
Otaheke-Sth	N	82 (cr32)	90	0.75 ± 0.23	82 (cr32)	550 ± 170	0.41 ± 0.12	460	0.37 ± 0.11	767 ± 460	25[c]	5	Sth
Rangatira[e]	N												Sth
Rangitikei	R	48 (tan26)	175	1.46 ± 0.44	33 (bm5)	650 ± 170	0.48 ± 0.14	475	0.39 ± 0.12	1570 ± 300	27	20	45
Tangimoana[f]	N	45 (cr25)	33	0.28 ± 0.08	45 (cr25)					240 ± 50	13	12	
Te Horo[f]	N	53 (cr61)	50	0.42 ± 0.13	38 (bm1-1)					410 ± 50	37	25	
Waimahora[d]	R									280	43	12,13,12	
Wairaka-Nth	N	78 (cr30)	20	0.17 ± 0.05	74 (cr62)	270 ± 50	0.20 ± 0.06	250	0.20 ± 0.06	300	15	10	25[c]
Wairaka-Sth[e]	N												Sth
Waitarere	R	82.5 (cr31)	71	0.59 ± 0.18	82.5 (cr31)	430 ± 125	0.32 ± 0.1	359	0.29 ± 0.09	480 ± 70	55[c]	21, 24[c]	Sth
Cumulative (KMFS reverse faults only)			590	4.92 ± 1.48	40	2430 ± 480	1.80 ± 0.50	1840	1.50 ± 0.45	3460 ± 700			
Whangaehu[g]	N?	15.5 (cr8)	40	0.33 ± 0.1	11 (m112)	120 ± 25	0.09 ± 0.03	80	0.07 ± 0.02	280	44	15,15,5	
Santoft[g]	R	38 (ea10)	80	0.67 ± 0.2	52 (cr26)	330	0.24 ± 0.07	250	0.20 ± 0.06	370	42	7	

[a]The maximum throws in meters for the H1 (Th.H1) and H4 (Th.H4) horizons are located at distances of L.H1 and L.H4, respectively, on the strike-parallel projection axis (distance in km; Figure 6). The MCS line on which the measurement is made is indicated (line); TR.H1 and TR.H4 are maximum throw rates in mm yr^{-1} for the last 120 and 1350 kyr periods, respectively. Rates are calculated at positions L.H1 and L.H4 for H1 and H4 horizons, respectively; TR.H4-H1 is the throw rate in mm yr^{-1} for the period 120–1350 ka, corresponding to the differential throw Th.H4-H1 measured between H4 and H1. Th.H4-H1 and TR.H4-H1 are calculated at position L.H4, i.e., at the same position as the maximum H4 throw. Th.Bas is maximum vertical offset of basement horizon. Fault lengths are given as follows: L1, maximum offshore fault length; L2, minimum fault length; multiple values indicate multiple segments or strong strike changes; L3, total maximum fault length including estimates of onshore sections.

[b]Interpolated values (e.g., where H4 is eroded or not deposited).

[c]Fault extends outside the study area, hence the length is under-estimated.

[d]Measurements included in Mascarin Fault.

[e]Slip rate and fault length not representative as fault mostly outside the study area.

[f]H4 not present.

[g]These faults do not belong to the KMFS.

largest throw of the H4 (1350 ± 40 ka) horizon in the KMFS, with a maximum 1050 ± 210 m offset, yielding a long-term throw rate of 0.78 ± 0.23 mm yr^{-1} (Table 2 and Figures 7–10). Tilted layers between the Mascarin Fault and the Waimahora and Hokio faults to the west and the M5 subsidiary fault to the east are likely to reflect the fact that displacements are being relayed between the faults. Because of the proximity of these faults we have attributed the throws across the Waimahora and M5 faults, as well as the vertical height difference associated with the tilted layers, to the total throw of the Mascarin Fault. We believe this measurement reflects the total amount of localized displacement associated with the Mascarin Fault at depth for each of the corresponding time periods. The dip of the Mascarin Fault, as measured above basement on depth-converted profiles, is 70° ± 5°.

[25] The Mascarin Fault is identified on all seismic lines north of Kapiti Island. Toward Kapiti Island, the Mascarin Fault only displaces the base of the sedimentary sequence and the basement horizon (MCS line CR31, Figure 10). Northward, from MCS line CR20, the Mascarin Fault splays into four subsidiary faults (M1 to M4), which correlate onshore with the Turakina Fault System [*Anderton*, 1981] (Figure 2).

[26] Throw profiles for the upper five basin-wide horizons (H1–H5) and the basement reflector along the Mascarin Fault (Figure 11) are strongly asymmetric, with maximum throws occurring toward the northern limit of the study area. Between 10 and 20 km along strike (i.e., at the northern end of the fault), high variability in the throw profiles for H2 and older horizons is related to insufficient data coverage across the M1 to M4 faults. The throws are maximum values where all faults are sampled (e.g., at the 12-km mark) and minimum where the easternmost faults are not imaged on seismic profiles. This indicates that vertical displacement is distributed onto the Mascarin Fault and its associated splays (M1 to M4) as the fault approaches the coast to the north. We assume that the M1 to M4 faults merge at depth, and therefore that the maximum throw of 1050 m at 17 km along strike (Figure 11) is representative of the displacement occurring at depth on the Mascarin Fault.

[27] Between 20 and 40 km along strike, throw profiles for the Mascarin Fault have low gradients, possibly suggest-

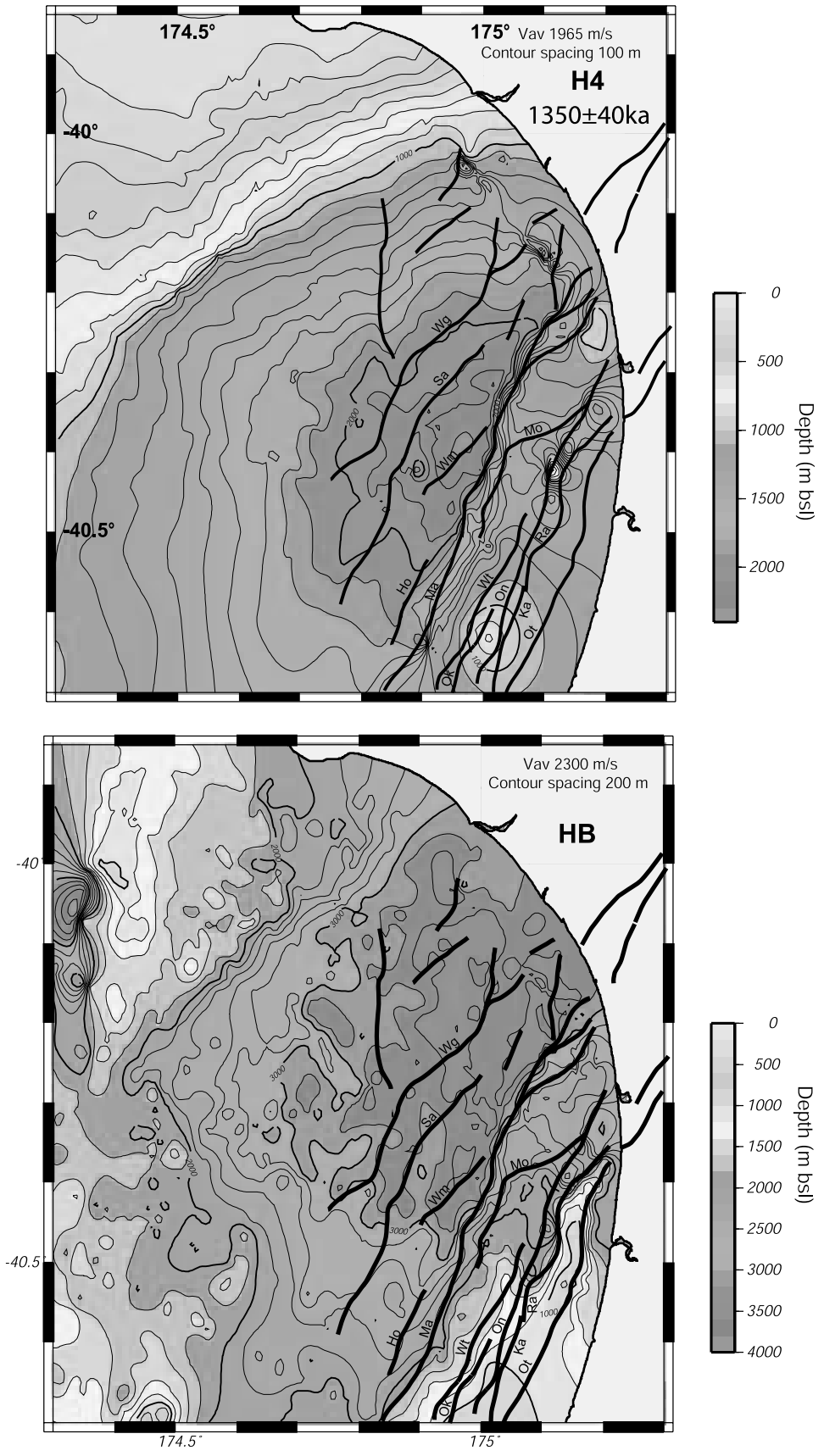
174.5°
175°
Vav 1965 m/s
Contour spacing 100 m
H4
1350±40ka
-40°
-40.5°
Wg
Sa
Mo
Wm
Ra
Ho
Ma
Wl
On
Ka
Or
Ok
0
500
1000
1500
2000
Depth (m bsl)
Vav 2300 m/s
Contour spacing 200 m
HB
-40
-40.5
174.5°
175°
0
500
1000
1500
2000
2500
3000
3500
4000
Depth (m bsl)

Figure 6

ing a well-established fault segment. Between 40 and 65 km, throws decrease rapidly, although there are no measurements between 67 and 83 km along strike. We estimate a maximum offshore length of 66 km (Table 2) for the Mascarin Fault. Because of the possible southward continuation of the fault beyond the study area, this distance may be underestimated. A minimum fault length of 42 km is interpreted between 15 and 55 km where there is improved control on delimiting the fault due to a seismic line spacing of <2 km.

5.2. Central West KMFS: Waitarere, Okupe, and Moana Faults

[28] The Waitarere and Okupe faults (new names) are subparallel, west dipping reverse faults that are no more that 3 km apart (Figure 5). Both faults divide into north and south segments, with the southern segments extending outside the study area. The Moana Fault (new name) dips steeply (>60°) to the west and is also divided into north and south segments, with the northern segment diverging markedly from the regional strike of the fault system, and linking with the Onepoto Fault to the east. Maximum throws of the H4 horizon along the Waitarere and Okupe faults are 430 ± 125 and 270 ± 54 m, respectively, yielding throw rates of 0.32 ± 0.1 and 0.20 ± 0.06 mm yr^{-1}, respectively (Figure 12 and Table 2). A maximum long-term throw rate of 0.30 ± 0.09 mm yr^{-1} is derived along the Moana Fault from an interpreted H4 maximum throw of 400 ± 80 m (Figure 12).

[29] At its northern end, the Waitarere Fault overlaps the southern end of the Moana Fault for ~7 km. The interplay between the Waitarere, Okupe and Moana faults are best illustrated on the throw profiles (Figure 12). The Moana Fault and the northern segments of the Waitarere and Okupe faults are ~20 km long, and their throw profiles are symmetrical about the point of maximum throw, forming conspicuous bell-shaped profiles. The points of maximum throw for each of these three faults do not change with time, indicating that (1) the fault geometry did not vary and strain was accommodated in a constant manner over the evolution of the faults; and (2) the faults interact constructively and transfer strain between each other. The maximum throw along the Waitarere Fault at ~57 km (Figure 12) along strike corresponds to the spatial gap between the Okupe and Moana faults, and maximum throws along the Okupe (72 km) and Moana (38 km) faults occur on either side of the Waitarere Fault northern segment. We interpret these observations as indicating that the lack of activity on the Waitarere Fault is matched by activity on the Moana and Okupe faults, so that there is conservation of displacement across the three faults.

[30] The H1 to H5 cumulative throw profiles for the Moana, Okupe and Waitarere faults do not have bell shapes as individual throw profiles do, with the profile minima corresponding to individual fault tips (Figure 12c). Similar throw profile irregularities have been associated with growth by fault linkage in normal fault systems [*Cartwright et al.*, 1995; *Cowie and Roberts*, 2001]. This suggests that fault linkages probably exist between the Waitarere, Okupe, and Moana faults. Although there is no identified hard linkage in the sedimentary sequence, we cannot discount that this happens within the basement.

5.3. Central East KMFS: Onepoto, Kapiti, Rangitikei, and Tangimoana Faults

[31] The Onepoto Fault (new name) is a reverse fault that runs from the mouth of the Rangitikei River to Kapiti Island, with a length of ~45 km. In its southern part, the Onepoto Fault runs along the summit of the northward plunging basement high that emerges at Kapiti Island, and is characterized by small displacements (<50 m) of the basement horizon (Figure 10). The fault is likely to extend along the west coast of Kapiti Island and the uplifted block of Kapiti Island indicates that the fault is upthrown to the east. This sense is opposite to that observed along the Onepoto Fault as it develops northward from Kapiti Island into a steep, west dipping reverse fault, with displacements within the Plio-Pleistocene sedimentary sequence occurring north of 67 km along strike. The fault dip is greater than 70°. The maximum throw of 590 ± 110 m across H4 yields a throw rate of 0.44 ± 0.13 mm yr^{-1} for the last 1350 kyr. The maximum throw of 690 ± 220 m on acoustic basement occurs at the northern end of the fault (Figure 13 and Table 2).

[32] The Kapiti and Rangitikei faults run no more than 3 km to the east of, and parallel to, the Onepoto Fault (Figure 5). Both faults are subvertical (Figures 8 and 9). Reverse displacement is interpreted along the northern portion of the Kapiti Fault, but along the southern part of the fault, poor resolution, shallow basement and reverberated energy in the seismic reflection profiles hamper identification of the sense of displacement. Throws along the Kapiti Fault vary rapidly, with a maximum basement offset of 430 ± 60 m at 72 km along strike, decreasing to less than 100 m at 68 km (Figure 13). The northern termination of the Kapiti Fault is approximately coincident

Figure 6. Isodepth maps for horizon H4 (1350 ka) and the basement reflector (HB) as identified from interpretation of MCS data. Two-way travel times to each horizon were converted to depth using the average velocities indicated in the top right corner of each plot. Average velocities (Vav) were compiled as the weighted average of interval velocities calculated from stacking velocities picked during processing of industry and NIWA TAN MCS data. Stacking velocities from the CR survey are discarded as unreliable. The relative errors on depth are similar to that of velocities (30%) as the error on picking time is considered negligible. Faults interpreted in this study (Figure 5) are superimposed on each map and designated by the following abbreviations: Wg, Whangaehu; Sa, Santoft; Wm, Waimahora; Ho, Hokio; Ma, Mascarin; Mo, Moana; Wt, Waitarere; On, Onepoto; Ok, Okupe; Ra, Rangitikei; Ka, Kapiti; Ot, Otaheke. See color version of this figure at back of this issue.

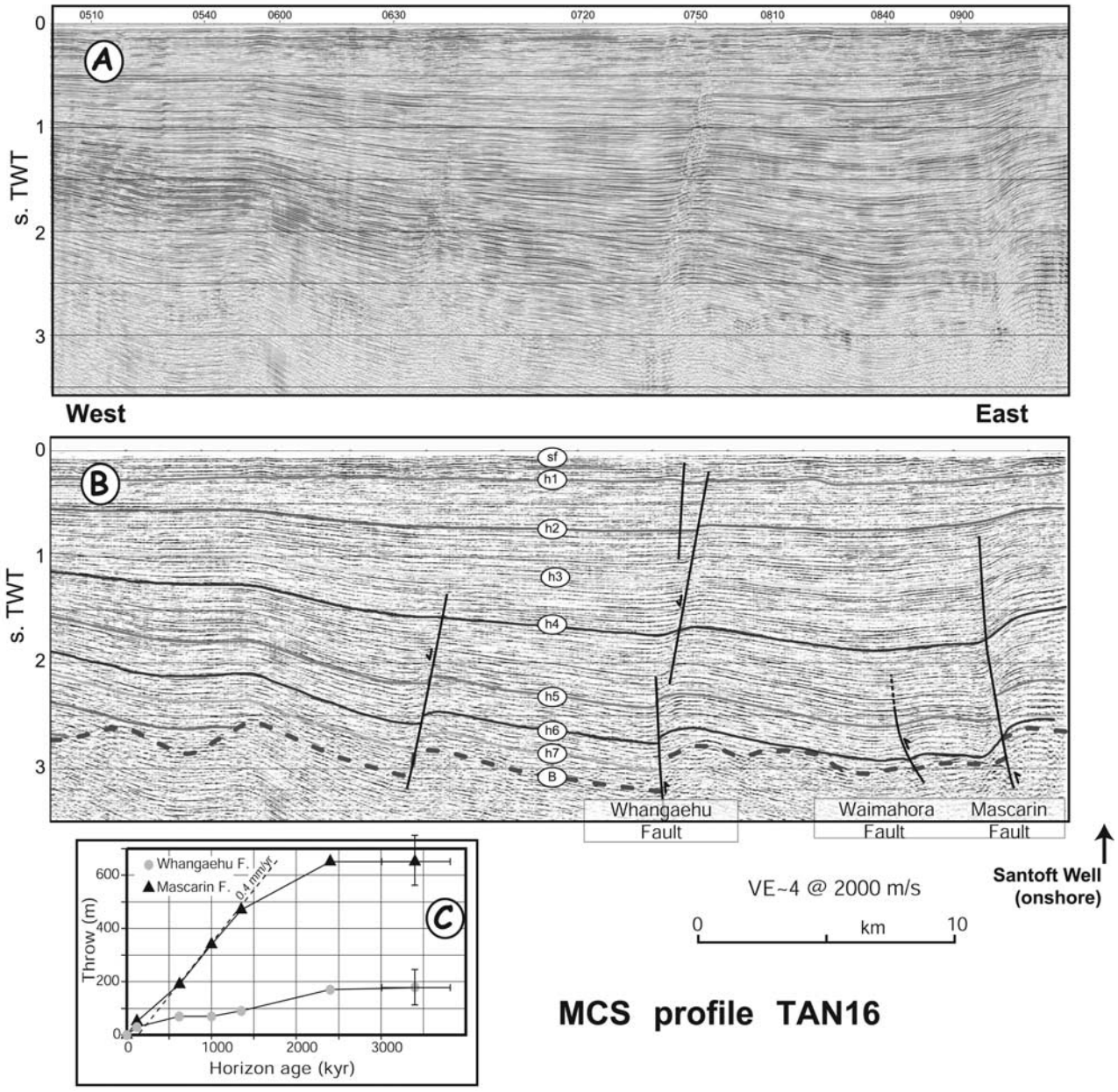

Figure 7. MCS profile TAN16 across the northern part of the KMFS. (a) Uninterpreted data. (b) Interpretation of seven key sedimentary horizons (h1–h7), seafloor (sf), and basement (B). Profile location is shown on Figures 4 and 5. (c) Time (age horizon ages) versus throw profiles for the Mascarin and Whangaehu faults. The Whangaehu Fault is located in the central part of the SWB; hence it is not part of the KMFS and was not used in subsequent calculations of cumulative throws and rates. Fault names are indicated at bottom of the interpreted profile. See color version of this figure at back of this issue.

with the southern tip of the reverse Rangitikei Fault. The maximum possible overlap of the two faults, in map view, is ~4 km. Normal faults in the hanging wall (west) of the Kapiti Fault only affect the sedimentary sequence, and are interpreted as representing secondary bending moment faults. These normal faults offset the seafloor (S. D. Nodder et al., manuscript in preparation, 2005).

[33] The largest displacement of H4 along the Rangitikei Fault (650 ± 170 m) yields a long-term throw rate of 0.48 ± 0.14 mm yr^{-1} (Table 2). Basement offsets vary significantly along the Rangitikei Fault (Figure 13) but are systematically much larger than that measured for H4. The maximum throw of 1570 ± 300 m along the Rangitikei Fault is the largest vertical displacement measured in the KMFS. The

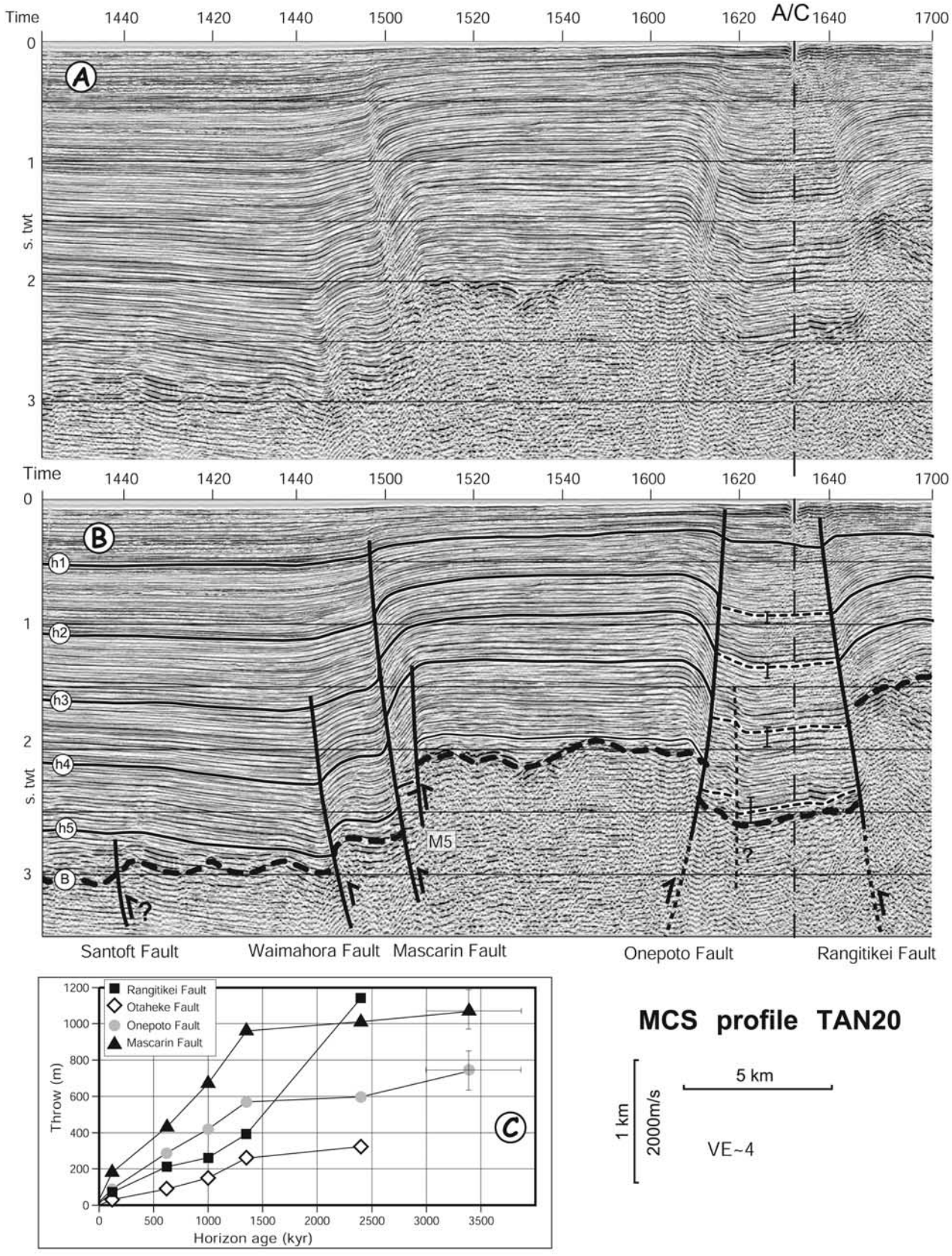
Time
1440
1420
1440
1500
1520
1540
1600
1620
A/C
1640
1700
A
B
s. twt
h1
h2
h3
h4
h5
B
M5
Santoft Fault
Waimahora Fault
Mascarin Fault
Onepoto Fault
Rangitikei Fault
Rangitikei Fault
Otaheke Fault
Onepoto Fault
Mascarin Fault
Throw (m)
Horizon age (kyr)
C
MCS profile TAN20
5 km
1 km
2000m/s
VE~4

Figure 8

Rangitikei and Onepoto faults converge upward, thus defining the walls of a ~3-km-wide, 27-km-long basin, whose floor is in the footwalls of both faults. This geometric relationship is best explained by inversion of a preexisting horst structure. Both faults have displacements of the same magnitude for horizons H1 to H4, but the basement maximum offset on the Rangitikei Fault remains much larger than that on the Onepoto Fault. Throws between H4 and the basement horizon represent approximately 60% and 15% of the total throws on the Rangitikei and Onepoto faults, respectively, which suggest that initiation of reverse faulting occurred before H4 on the Rangitikei Fault and that, subsequently, both faults have had similar development.

[34] Throw profiles for the Onepoto and Rangitikei faults are highly asymmetric with the maximum throws occurring in the northern parts of the faults (Figure 13). The Rangitikei Fault throw profiles have low gradients for H1 to H3, while the profile for H4 is very irregular with low gradients in the central part (~33–48 km) and high gradients at the transition with the Kapiti Fault. Low gradients indicate similar displacements along the length of the fault. Small throws along the Onepoto Fault (e.g., at 55 km, Figure 13) correspond to high throws on the Kapiti Fault, and the increase in throw along the Kapiti Fault south of 67 km correspond to a rapid decrease of vertical displacement along the Onepoto Fault. Similarly as for the Waitarere, Okupe and Moana faults, we infer that these observations indicate that fault interactions are occurring between the Onepoto, Rangitikei and Kapiti faults, so that displacement is preserved along strike of the three faults.

[35] The Tangimoana Fault is a normal fault located in the hanging wall (east) of the Rangitikei Fault. The maximum throw across H1 and the basement horizon along the Tangimoana Fault are 33 ± 5 m and 240 ± 50 m, respectively. H4 is not identified across the Tangimoana Fault. The fault is associated with steep slopes at the seafloor, which are interpreted as representing fault scarp.

5.4. Southeast KMFS: Otaheke, Wairaka, Rangatira, and Te Horo Faults

[36] In the coastal part of the KMFS, we identify the Otaheke, Te Horo, and Wairaka faults (new names), as well as the Rangatira Fault as it extends north of Kapiti Island, and along the eastern shore of Kapiti Island, as first described by *Moore and Francis* [1988]. All faults are subvertical. The Otaheke and Wairaka faults divide into northern and southern segments. The northern Otaheke Fault has reverse displacement associated with it, while all the other faults in this group are extensional structures. At its northern end the Otaheke Fault splits into two subvertical faults, which only affect the sedimentary sequence (Figure 9). The southern Otaheke, Wairaka, and Rangatira faults accommodate the formation of the graben between Kapiti Island and the coast. The basement is not imaged beneath the graben, but the minimum sediment thickness is 1.2 s (1200 m, Figures 6 and 10).

[37] There are some unresolved issues related to the poor quality of the seismic data associated with shallow water depths, as well as a lack of seismic profiles close to the coast. In particular, there are poor constraints on the depths of horizons east of these faults, which result in high uncertainties associated with measured fault throws. It is also unclear as to whether the Rangatira Fault merges northward with the Otaheke Fault or the Kapiti Fault, and whether the southern and northern Wairaka fault segments are linked. These ambiguities do not, however, impact on the regional structural pattern as described here.

[38] Throw profiles for the northern and southern Otaheke faults are irregular and the profiles for H1 to H3 are flat, suggesting uniformly distributed deformation along the length of the fault (Figure 14). Both the northern and southern segments have similar maximum throws for H4 (570 ± 100 and 550 ± 170 m, respectively), yielding a long-term throw rate of ~0.42 ± 0.13 mm yr^{-1} (Table 2). The maximum basement reflector offset is also similar for both segments (770 ± 460 m). The Wairaka and Te Horo fault throw profiles are poorly constrained, with few measurements and incomplete sampling of the faults. There is a clear increase in vertical displacement from H3 to H4 on the northern part of the Te Horo Fault, which is marked by an obvious decrease for the same period on the Otaheke Fault.

5.5. Central SWB Basement Faults: Whangaehu and Santoft Faults

[39] The Whangaehu and Santoft faults are not part of the KMFS but contribute to the total strain accommodation in the upper plate of the Hikurangi subduction margin. Our interpretation generally agrees with the basement faults as interpreted by *Anderton* [1981] in the central part of the SWB. Both Whangaehu and Santoft faults (new names, Figure 5) displace the top of the basement reflector and have steep dips (65–75°). Along the Whangaehu Fault, offsets of the H4 horizon and above indicate normal displacement while offsets at depth indicate reverse faulting (Figure 7). The proximity and similarity with the reverse Mascarin Fault to the east suggests that the Whangaehu Fault represents an inverted normal fault (see discussion). H1 offset is 40 ± 10 m along the Whangaehu Fault which confirms ongoing tectonic activity. Normal faults associated with the Whangaehu Fault are interpreted as bending moment faults associated with growth of young anticlines as has been interpreted onshore [*Pillans*, 1990]. The Santoft Fault (Figures 5 and 7) is a reverse fault that mostly displaces

Figure 8. MCS profile TAN20 across the northern part of the KMFS. (a) Uninterpreted data A/C, altered course. (b) Interpretation of five key sedimentary horizons (h1–h5) and basement (B). Profile location is shown on Figures 4 and 5. (c) Profiles of time (as horizon ages) versus throw for four faults of the KMFS. Fault names are indicated at bottom of the interpreted profile.

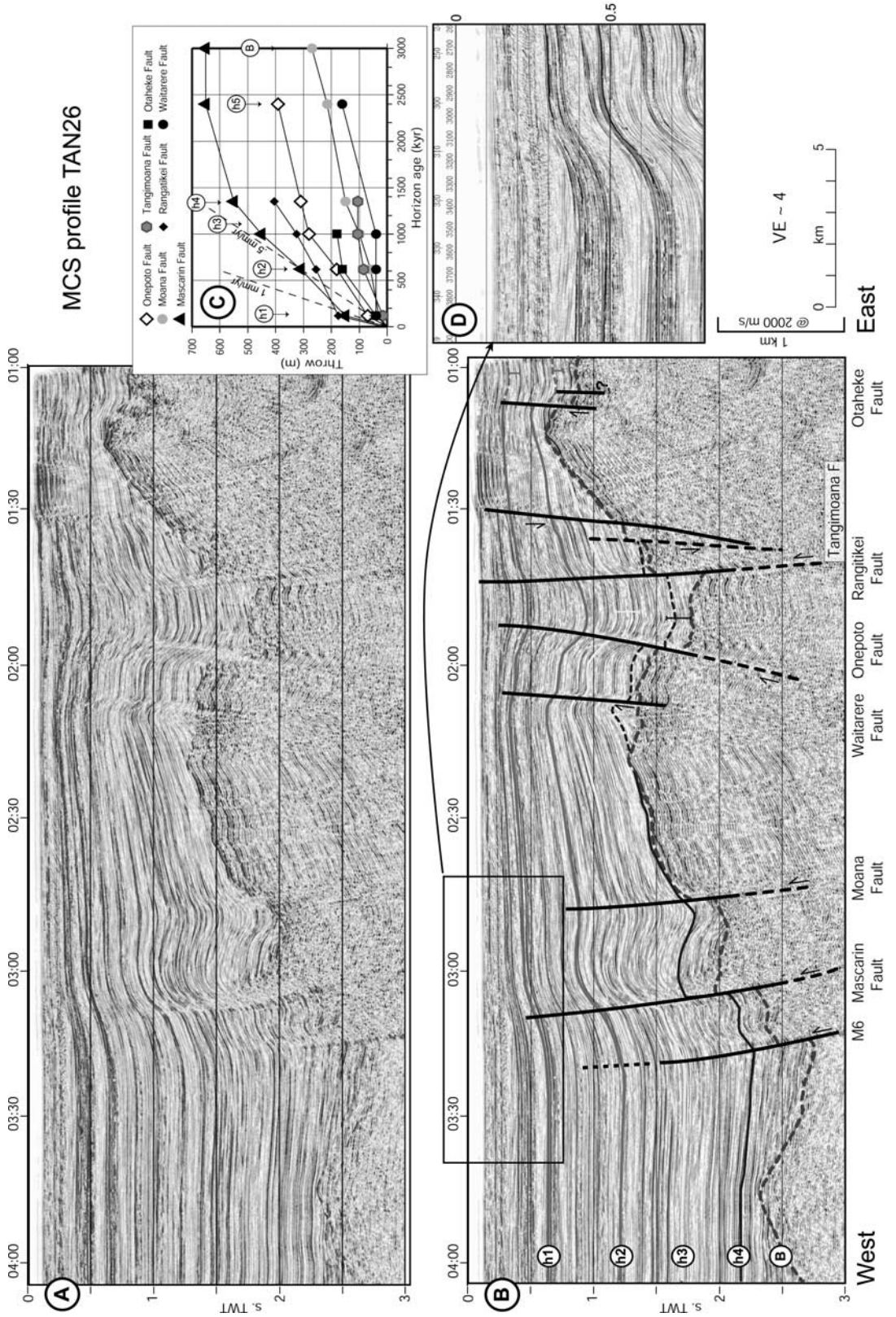
MCS profile TAN26
A
B
C
D
s. TWT
Throw (m)
Horizon age (kyr)
~ 1 mm/yr
~ 5 mm/yr
Onepoto Fault
Tangimoana Fault
Otaheke Fault
Moana Fault
Rangatikei Fault
Waitarere Fault
Mascarin Fault
h1
h2
h3
h4
h5
B
M6
Mascarin Fault
Moana Fault
Waitarere Fault
Onepoto Fault
Tangimoana F
Rangitikei Fault
Otaheke Fault
West
East
1 km
@ 2000 m/s
VE ~ 4
km

Figure 9

the basement reflector, with fault propagation folding visible up to the H3 horizon.

6. Discussion

[40] Well-constrained throw profiles of individual faults in the contractional KMFS provide an opportunity to discuss the spatial and temporal evolution of the faults over the last 3 Myr. In the following, we demonstrate that the coherent fault model, as developed for normal fault populations by *Walsh et al.* [2003], can be applied to the reverse fault population of the KMFS. We justify the interpretation of the present-day KMFS as a mature, coherent, contractional fault system, with fault lengths initiated early in the evolution of the fault zone by reactivation of preexisting extensional structures under a constant regional strain regime. The strain and strain rates across the upper plate are then estimated over the last 3 Myr in the geodynamic context of the highly coupled plate interface of the Hikurangi subduction margin.

6.1. Origin of the KMFS

[41] The very steep fault dips ($\sim$70°) observed within the KMFS, are most probably associated with tectonic inversion, whereby preexisting normal faults controlling basin floor subsidence are reactivated as reverse structures. Very high reverse fault dips are best achieved by normal fault reactivation or in strike-slip settings [e.g., *Harding*, 1990; *Hayward and Graham*, 1989; *Nielsen and Bayer*, 2003]. The lack of strike-slip deformation (see 6.3.1), normal faults in the central part of the SWB (e.g., the Whangaehu Fault) and on the Patea-Tongaporutu High on the western flank of the SWB (NIWA unpublished data), as well as the characteristic inverted horst identified between the Onepoto and Rangitikei faults (Figures 8 and 9), further substantiate our interpretation that the KMFS originate from reactivation of preexisting extensional structures.

[42] The timing of the extensional phase in the KMFS cannot be constrained fully since sediments older than H5 (2400 ka) are not preserved in the fault hanging walls due to erosion or nondeposition (Figures 7–10). Widespread extension took place in the New Zealand region in Late Cretaceous to early Eocene and late Eocene to Oligocene, associated with normal faulting [e.g., *Kamp*, 1986; *Spörli*, 1980]. This phase of normal faulting predates the formation of the SWB and could have facilitated the initial subsidence of the SWB.

[43] Furthermore, the broad-scale geometry of the sedimentary units suggests there were two major phases of subsidence during the evolution of the SWB: a pregrowth phase from 3.8 to 1.35 Ma and a syngrowth phase from 1.35 Ma to present-day [*Proust et al.*, 2005]. *Stern et al.* [1992] proposed that the SWB subsidence is caused by the pull-down effect of the subducting Pacific Plate and sediment loading of the lithosphere. Since it is unlikely that sediment loading would have been sufficient to augment the tectonic subsidence in the early history of the SWB, subsidence was probably homogeneous initially across the basin and has been facilitated by pervasive normal faulting. This first phase of subsidence occurred prior to the formation of horizon H4 (1350 ± 40 kyr, Table 1), which marks a significant shift in the depositional architecture of the basin with conformable units deposited prior to this time below the unconformity at the base of the Castlecliffian section [*Proust et al.*, 2005]. The long-term subsidence rate from 3000 ka to 1350 ka (i.e., H7 to H4) is moderately low at 0.7 ± 0.5 mm yr^{-1}.

[44] Above horizon H4, pervasive downlapping and basinward thickening of basin fill sediments to the southeast [*Proust et al.*, 2005] indicate a second phase of subsidence that was differential, localized and facilitated largely by reverse faulting in the KMFS. During this time subsidence rates in the KMFS accelerated, allowing rapid infilling of the SWB and accentuating the tectonically driven subsidence by sediment loading. The long-term subsidence rate of 1.7 ± 0.5 mm yr^{-1} in the SWB has increased since deposition of H4, as constrained by the maximum depth of H4 (2300 ± 460 m, Figure 6).

6.2. Analysis of a Coherent Fault System

6.2.1. Distribution of Cumulative Throw

[45] Fault population analysis in extensional settings have shown that normal faults have vertical displacement profiles symmetrical about the points of maximum displacement, and this has been used to help constraining the history of fracturing in extensional sedimentary basins [e.g., *Meyer et al.*, 2002]. Furthermore, the constant length model of fault growth [*Walsh et al.*, 2003] has been derived largely from normal fault data sets. In contrast, there is a lack of similar analysis of reverse fault populations, and such model has not been recognized previously in contractional settings.

[46] All fault segments enclosed entirely within the survey area (e.g., Hokio, Moana, northern Waitarere, and northern Okupe faults) have throw profiles that are sym-

Figure 9. MCS profile TAN26 across the central part of the KMFS. (a) Uninterpreted data. (b) Interpretation of four key sedimentary horizons (h1–h4) and basement reflector (B). The southward rising of the graywacke basement results in the progressive thinning of the sedimentary sequence south of the depocenter (Figure 6) and the disappearance of key horizons older than H4. The colored error bars reflect the large uncertainty in the positions of the key horizons, associated with the lack of N-S oriented tie lines between the Onepoto and Rangitikei faults, as well as west of the Otaheke Fault. The question mark indicates uncertainty as to whether the subvertical fault in the footwall of the Otaheke Fault is reverse or normal. (c) Time (as horizon ages) versus throw. (d) Enlargement of near-surface layers showing fault growth and onlap features in the footwall of the Mascarin Fault indicating faulting activity post-H1 (120 ka) horizon. Note also the westward progradation of sediment. Profile location is shown on Figures 4 and 5. Fault names are indicated at bottom of the interpreted profile. See color version of this figure at back of this issue.

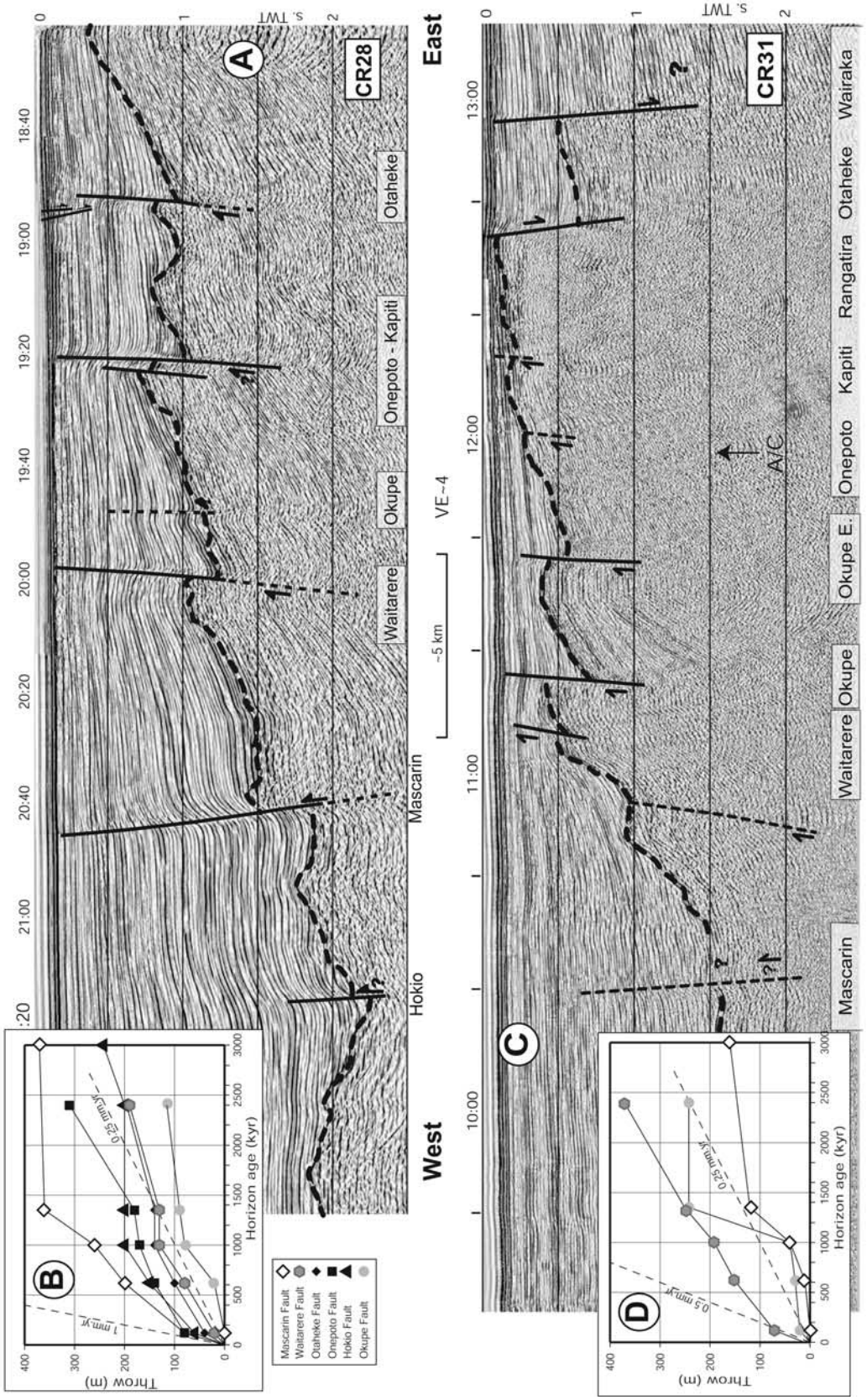
A
CR28
CR31
C
D
B
West
East
Hokio
Mascarin
Waitarere
Okupe
Onepoto - Kapiti
Otaheke
Okupe E.
Onepoto
Kapiti
Rangatira
Otaheke
Wairaka
~5 km
VE~4
AJC
s. TWT
Throw (m)
Horizon age (kyr)
1 mm.yr
0.25 mm.yr
0.5 mm.yr
Mascarin Fault
Waitarere Fault
Otaheke Fault
Onepoto Fault
Hokio Fault
Okupe Fault

Figure 10

metrical about the point of maximum throw (Figures 12 and 13), resulting in bell-shaped profiles. In contrast, other faults extending outside the study area (e.g., Mascarin, Onepoto, and Rangitikei faults) have clear asymmetrical throw profiles, with the maximum offsets occurring at their northern ends (Figures 11 and 13). The cumulative throw profiles, for horizons H1 to H4 and basement, summed across the entire ~25-km-wide KMFS, are symmetrical about their points of maximum throw (Figure 15). The stable locations of the points of maximum throw over time, on all individual and cumulative throw profiles suggest that the faults have not changed their locations markedly since their inception as reverse structures. The steep gradients along the northern half of the cumulative profiles (10–35 km) is probably related to the lack of data for the Onepoto and Rangitikei faults as they extend onshore (i.e., in the sense of fault censoring as given by, e.g., *Meyer et al.* [2002] in the Timor Sea). Nevertheless, the general bell shape of the cumulative profiles, together with the throw profiles of fully surveyed faults, suggest that reverse faults in the KMFS follow a model with maximum displacement occurring toward the middle of the fault segment. In extensional settings, bell-shaped cumulative displacement profiles and constant positions of maximum displacements and fault terminations have been ascribed to coherent, fully developed fault systems [e.g., *Meyer et al.*, 2002; *Walsh et al.*, 2003]. From the similarities between coherent normal fault systems and the KMFS, we propose that the KMFS represents a mature, coherent, contractional fault system, with fault lengths likely to have been initiated early in the evolution of the fault zone. The early acquisition of fault lengths is consistent with reactivation of preexisting extensional structures under a constant regional strain regime.

6.2.2. Displacement-Length (D/L) Scaling

[47] The irregular cumulative throw profiles for the Moana, Okupe, and Waitarere faults (Figure 12c) as well as for the Onepoto and Rangitikei faults (Figure 13) imply that linkages occur between faults, and that this process may have contributed to the rapid growth of the fault system to its present-day length. If this is correct, the minima in the cumulated throw profiles for the KMFS could indicate segment boundaries of the linked fault array (Figure 15) [see also *Cowie and Scholz*, 1992].

[48] In order to constrain the maximum lengths of the faults that extend onshore to the northeast (e.g., Mascarin, Onepoto, and Rangitikei faults), we used the fault half lengths, as defined by their respective asymmetric throw profiles, and measured from the southern tip of each fault to the point of maximum throw (Table 2). This is justified as all faults in the system are assumed to be fully developed and those faults that are well constrained by the offshore data have symmetrical throw profiles about their point of maximum throw. The Mascarin Fault has a minimum length of 42 km as constrained from its offshore throw profiles (Figure 11). The fault correlates onshore with the Turakina Fault, which extends up to 80 km to the northeast (Figure 5) [*Anderton*, 1981], and we therefore derive a maximum total length of 92–102 km for the Mascarin-Turakina fault. The Onepoto, Rangitikei, and northern Otaheke faults have maximum offshore lengths of 78, 27, and 38 km, respectively, with the two former faults displaying asymmetric throw profiles with maximum values to the northeast, which support their extension onshore. The maximum lengths for the Onepoto Fault (90 km), the Otaheke Fault (50 km), and the Rangitikei Fault (45 km) are constrained by correlations with faults to the northeast identified on onshore seismic profiles and by the characteristically large basement offsets observed across the Rangitikei Fault both onshore [*Anderton*, 1981] and offshore (this study).

[49] Displacement-to-length (D/L) relationships (Figure 16) show that all basement faults in the KMFS, with the exception of the Rangitikei Fault, have lower maximum throw with regard to their maximum lengths compared with that empirically derived for normal fault populations [*Cartwright et al.*, 1995; *Schlische et al.*, 1996]. *Cartwright et al.* [1995] and *Schlische et al.* [1996] interpret D/L scatterplots for normal fault populations as a proportional logarithmic relation between displacement and length over 5 orders of magnitude. The relation may be described by a slope of between 1 and 2 for faults ranging in length from 100 m to 100 km. For all faults in the KMFS, the minimum fault lengths, L2 (Table 2), arrange along the empirical D/L log linear trend. This suggests either that maximum lengths (L1) were overestimated or that faults in the KMFS are underdisplaced relative to the global data set of faults. The latter interpretation possibly reflects the low contractional strain of the system. Future throw increase would result in the L1 fault length (best estimate, Table 2) to move vertically, closer to the linear trend of the global data set. Hence it is likely that individual faults show vertical fault growth (i.e., during fault evolution, faults attain and maintain constant lengths). This is shown for the Mascarin Fault by deriving incremental basement offsets at 1350, 1000, and 620 ka, for a constant 66 km fault length (Figure 17b). We realize, however, that there are considerable uncertainties in the fault properties and measurements obtained by this study and that this model will need further constraining by analyzing and comparing other similar systems.

6.3. Strain Analysis

6.3.1. Lack of Strike-Slip Deformation

[50] Our interpretation of the KMFS as a predominantly contractional fault system does not support a significant

Figure 10. (a) MCS profile CR28 across the southern part of the KMFS. (b) Profile of time (as horizon ages) versus throw for the faults interpreted in this profile. (c) MCS profile CR31 across the southern part of the KMFS, immediately north of Kapiti Island. (d) Profile of time (as horizon ages) versus throw for faults interpreted in this profile. Note the proximity of the graywacke basement to the seafloor. Only the basement (thick dashed line) is indicated. Profile locations are shown on Figures 4 and 5. Fault names are indicated at bottom of the profiles.

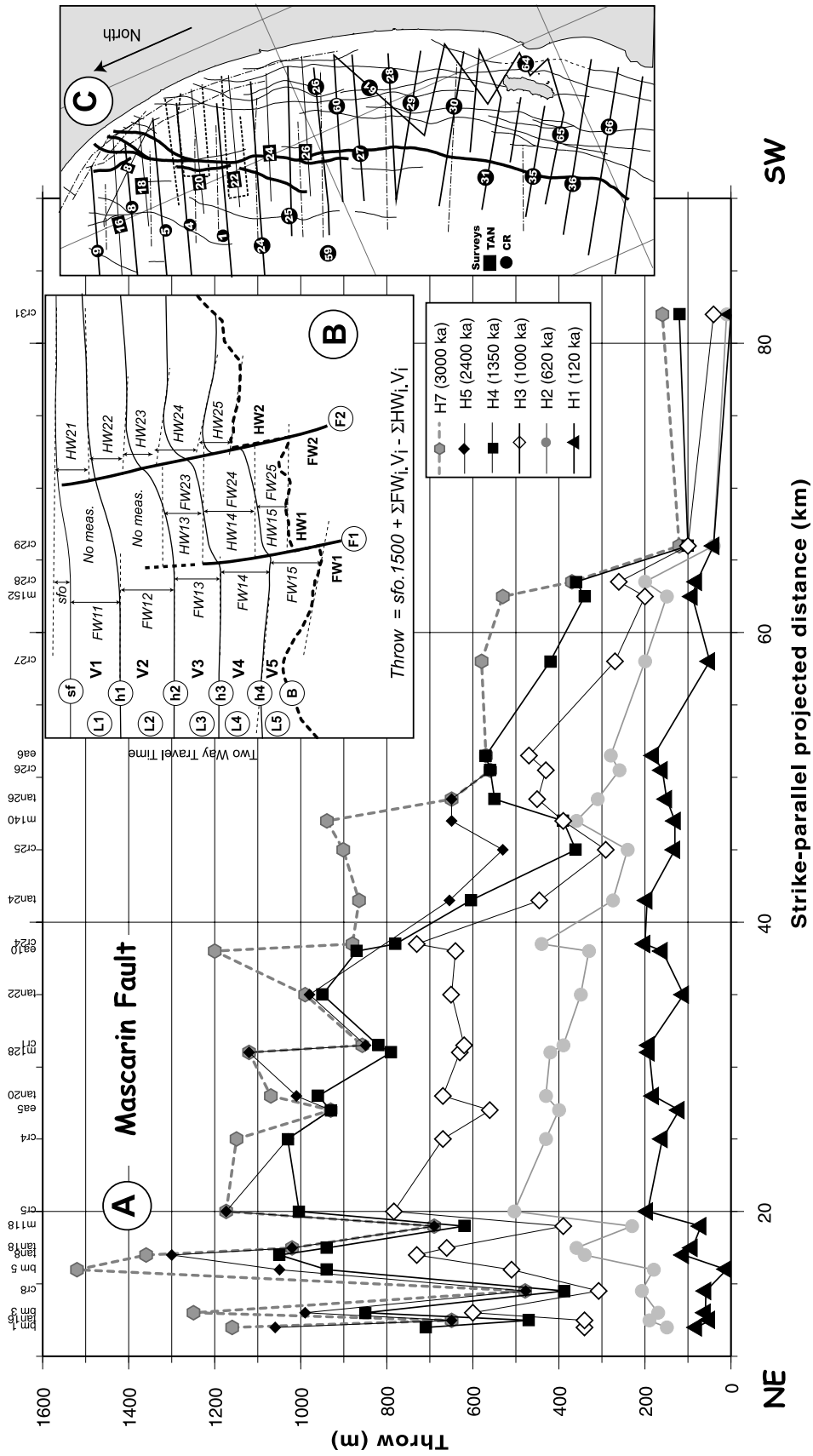
A
Mascarin Fault
B
C
North
Surveys
TAN
CR
H7 (3000 ka)
H5 (2400 ka)
H4 (1350 ka)
H3 (1000 ka)
H2 (620 ka)
H1 (120 ka)
Throw = sfo.1500 + ΣFWi.Vi - ΣHWi.Vi
Two Way Travel Time
Throw (m)
Strike-parallel projected distance (km)
NE
SW

Figure 11

component of strike-slip deformation. Although our structural interpretations are in agreement with that of *Anderton* [1981] in the northern half of the study area, there are marked differences with previous strike-slip interpretations of offshore faults in the KMFS describing: (1) flower structures [*Thompson et al.*, 1994]; (2) en echelon patterns [*Anderton*, 1981]; and (3) wrench faulting associated with strike-slip deformation [*Katz and Leask*, 1990]. It is acknowledged widely that interpretation of strike-slip motion from seismic reflection cross sections is particularly ambiguous [e.g., *Harding*, 1990; *Wilcox et al.*, 1973]. In the case of the KMFS, fault geometries, both in cross section and map view, do not resemble flower structures in that (1) faults often consist of a single trace; (2) fault dips do not change along strike, except in the southeastern part of the study area; and (3) there are no complex fault interactions apparent in seismic reflection cross sections (so-called positive or negative flower structures). Furthermore, we do not see small step-over basins or pop-up domes along and between individual faults while interpolation between seismic lines does not support en echelon fault patterns nor the occurrence of a throughgoing master fault, as observed in many well-developed wrench fault systems [*Harding*, 1990]. Finally, the faults do not display a braided pattern typical of many strike-slip fault zones, and overall the three-dimensional fault pattern of the KMFS is that of a series of consistently 60° to 75° dipping reverse faults, suggestive of convergent fault blocks.

[51] Some strike-slip deformation is possible, however, in the southern part of the KMFS, as suggested by (1) the transition from normal to reverse faulting along the Otaheke Fault; (2) the increase in fault interconnectivity toward Kapiti Island; (3) the possible along-strike change in dip of the Wairaka Fault; and (4) the subvertical dip of the normal faults to the southeast.

[52] Strike-slip deformation within the upper crust of southern North Island (e.g., Wairarapa, Wellington, Shepherd Gully, Pukerua, and Ohariu faults; Figure 3) accounts for 50–75% of the margin-parallel component of the Pacific-Australia relative plate motion. Up to 100% of the remaining strike-slip could be accounted for by oblique slip along the subduction interface [*Darby and Beavan*, 2001]. The only quantitative estimate of possible strike-slip along the offshore KMFS is derived strike-slip rates of 0.8–0.4 mm yr^{-1} along the Pukerua Fault [*Van Dissen and Berryman*, 1996], which may link northward with the Wairaka Fault. This estimate probably represents a maximum strike-slip rate for the Wairaka Fault as strike-slip rates inferred along the NIDFB and evidence of strike-slip deformation decrease northward in eastern North Island [*Beanland*, 1995].

[53] More constraints on the strike-slip to convergence budget across the plate boundary as a whole are required to better estimate strike-slip displacement along the KMFS. Certainly, more piercing points (i.e., seismic reflection profiles) or high-resolution bathymetric imagery along the faults, would help in quantifying strike-slip activity offshore. While we suggest that the amount of strike-slip displacement is likely to be a small component of the total displacement in the KMFS, a limited amount of strike-slip on such steep faults would facilitate fault reactivation [*Sibson*, 1995] and could therefore account for some of the reactivated history of faults within the KMFS.

6.3.2. Long-Term Dip Slip Rates

[54] Maximum throws can be identified on most faults in the KMFS from their bell-shaped displacement profiles. These provide an opportunity to calculate long-term throw and dip slip rates for the KMFS for the periods 0–1350, 0–120, and 120–1350 ka. Assuming a 65–70° average fault dip, the dip slip rates are 6.5–10% greater than the throw rates (Table 3). We believe that maximum throws were identified for all faults. Hence all rates discussed in this section are long-term maximum values. This is a significant improvement compared with two-dimensional geophysical surveys, which cannot provide information on slip rate variation along fault strikes and therefore cannot assign maximum rates to individual faults.

[55] Slip rates are characterized by a marked change observed for most faults at 120 ka, as well as a prominent inflection point at 1350 ka, as best exemplified for the Mascarin Fault (Figure 17a). The highest long-term dip slip rates in the offshore KMFS are found on the Mascarin Fault with 0.83 ± 0.25 mm yr^{-1} for the 1350 to 120 ka period, increasing to 1.77 ± 0.53 mm yr^{-1} from 120 ka to present. Little displacement occurred between 1350 and 3000 ka along the fault.

[56] Similar patterns of relative tectonic quiescence between 3000 ka and 1350 ka are suggested for the Moana, Otaheke and Okupe faults. The onset of significant fault activity may have been delayed by 350 kyr on the Onepoto Fault, as indicated by a lack of sediment accumulation, evident on profiles between 35 and 50 km along the

Figure 11. (a) Throw profiles along the strike of the Mascarin Fault for horizons H1 to H5 and H7. The basement reflector is given the age of H7 (3000 ka) as this is the oldest stratigraphic marker identified in the footwall of the KMFS. The origin (0 km) of the projection axis is at the coast on the northern end of the survey area (Figure 5). Approximate locations of seismic lines are indicated at the top of the diagram and on inset C (see also Figure 5). (b) Schematic drawing of the method used to incrementally measure fault throws. Fault throws are recorded as the differences in travel time between footwall and hanging wall horizon cutoffs and subsequently converted to vertical heights using average interval velocities generated from seismic and well data (see text). Measurements do not include decompaction of the growth sequence. Fault drag sometimes results in folding in the footwall and hanging wall. We consider fault drag as localized deformation associated directly with discrete displacement along the fault plane, and not as distributed deformation. Folding and warping directly above the fault is also considered to be associated directly with localized deformation on the fault and as accommodating part of the cumulative vertical displacement and shortening associated with the structure. (c) Lateral sampling along the Mascarin Fault indicated in this location map, showing the intersections of seismic lines with the fault.

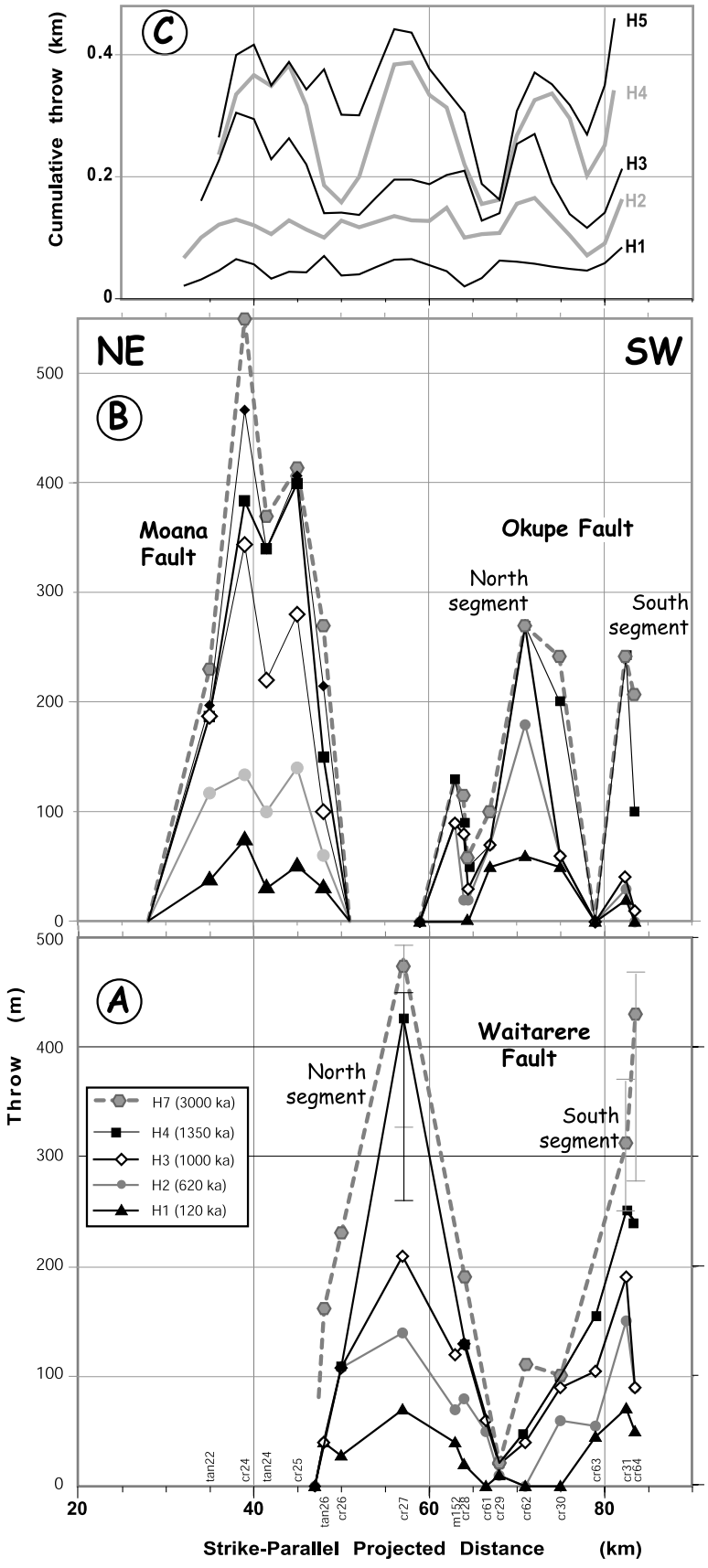
C
Cumulative throw (km)
0.4
0.2
0
H5
H4
H3
H2
H1
NE
SW
B
Moana Fault
Okupe Fault
North segment
South segment
500
400
300
200
100
0
A
Throw (m)
Waitarere Fault
North segment
South segment
H7 (3000 ka)
H4 (1350 ka)
H3 (1000 ka)
H2 (620 ka)
H1 (120 ka)
tan22
cr24
tan24
cr25
tan26
cr26
cr27
m152
cr28
cr61
cr29
cr62
cr30
cr63
cr31
cr64
20
40
60
80
Strike-Parallel Projected Distance (km)

Figure 12

projection axis (Figure 13), with most of the motion taken up at this time along the Rangitikei Fault. Large throws of ~150 m since 120 ka along the Onepoto Fault indicate a sudden increase in the dip slip rate to a maximum value of 1.33 ± 0.40 mm yr^{-1}, although overall the fault has exhibited only moderate dip slip rates with a maximum long-term value of 0.47 ± 0.14 mm yr^{-1} for the last 1350 kyr, especially on the northern sections of the fault. The Moana and Waitarere faults have long-term dip slip rates of 0.32–0.34 mm yr^{-1}, while values of ~0.20 mm yr^{-1} are characteristic of the Okupe and Hokio faults. The rates increase noticeably over the last 120 kyr for these two faults to ~0.6–0.8 mm yr^{-1}.

[57] The Rangitikei Fault seems to have operated quite differently during the evolution of the KMFS, with moderate to high sediment accumulation rates persisting through the early history of the fault with 650 and 1570 m vertical offsets for H4 (1350 ka) and basement (H7, 3000 ka), respectively, yielding a long-term dip slip rate of ~0.49 ± 0.15 mm yr^{-1}. This is interspersed with a period of relative quiescence between 1000 and 620 ka and followed by an intensification of slip rates, especially over the last 120 kyr to values close to 1.5 mm yr^{-1}. The Waitarere Fault also seems to exhibit a relatively long period of slow fault growth over the last 2.4 Myr, but overall slip rates (~0.3 mm yr^{-1}) are generally much lower than those estimated for the Rangitikei Fault over the same time period. The remaining faults within the offshore KMFS have long-term slip rates over the last 1.35 Ma of generally less than 0.3 mm yr^{-1}.

6.3.3. Timing of Deformation

[58] From the cumulative throws summed across reverse faults in the KMFS for horizons H1 to H4, we derived long-term throw rates across the entire KMFS along three transects at 20, 40 and 60 km along the strike-parallel projection axis (Figure 17b). Cumulative throw rates of 4.3 and 1.25 mm yr^{-1} for the 0–120 ka and 120–1350 ka periods, respectively, are observed at 40 km along strike. These values are slightly lower than the maximum cumulated rates of 4.9 and 1.80 mm yr^{-1} for the same periods, as calculated along the whole KMFS (Table 2). The vertical cumulative difference of more than 1000 m between the central transect (40 km) and the southern (60 km) and northern (20 km) ones is significant, even though the northern transect does not include the Onepoto, Rangitikei, and Otaheke faults since they extend onshore. This shows that the transect at 40 km is representative of the maximum offsets along of the KMFS.

[59] The first indication of deformation by faulting in the SWB occurs on the Rangitikei Fault where high throw rates of ~0.7 mm yr^{-1} were measured between 2400 and 1350 ka (Figure 8c), in contrast to negligible throws measured on most of the other faults in the KMFS over the same time period (Figures 7c, 8c, 9c, 10b, 10d, and 17a). Lesser amounts of activity were also apparent on the Onepoto and Waitarere faults over this initial period of KMFS deformation (Figures 10b and 10d). The maximum throw of 780 ± 340 m, estimated between the basement reflector and H4 along the Rangitikei Fault (Figure 12), provides an estimate of the minimum amount of inversion that has occurred on the fault since the inception of contraction across the KMFS.

[60] Contractional deformation had become pervasive in the KMFS by at least 1350 ka with deformation likely to have commenced some time between 1350 and 2400 ka since sedimentary units deposited prior to horizon H4 formation have been uplifted and deformed across the KMFS. Using cumulative throws versus time for reverse faults in the KMFS (Figure 17b), we infer an age of 1750 ± 400 ka for the initiation of the contractional phase. From 1750 ka to 120 ka, fault growth in the KMFS progressed at moderate rates of 1.25 ± 0.55 mm yr^{-1} with substantial amounts of deformation accommodated on the Mascarin Fault (Figures 8c, 9c, and 10b). The onset of contractional faulting at 1750 ka in the KMFS corresponds closely to the second phase of deformation identified in the forearc basin, to the east of the Axial Ranges [*Beanland et al.*, 1998; *Nicol et al.*, 2002].

[61] The final phase of faulting in the KMFS began at ~120 ka when throw rates on almost all structures increased substantially, as documented on the Mascarin Fault where dip-slip rates approximately doubled from ~0.8 mm yr^{-1} prior to 120 ka to ~1.77 mm yr^{-1} since this time (Table 3). This interpretation is dependent upon the age correlation of horizon H1 with the unconformity associated with the Rapanui Terrace Formation at 120 ka. The alternative age of 260 ka for H1 would results in throw rates of ~1.5 mm yr-1 for the whole 0–1350 kyr period. However, the younger age of 120 kyr for horizon H1 and the associated increase in faulting activity in the KMFS since this time is compatible with observations elsewhere in the plate boundary zone. *Lamb and Vella* [1987] indicate that shortening rates on Pleistocene fold structures in southeastern North Island have almost doubled since 100 ka, increasing to ~1.37 mm yr^{-1} from 0.6–0.9 mm yr^{-1} prior to this time, which is compatible with the 120 ka aged increase in deformation rates proposed in the KMFS. Offshore, in the forearc basin, *Barnes et al.* [2002] also suggest an increase in vertical slip rates on the Lachlan Fault from ~2 mm yr^{-1} prior to 120 ka to

Figure 12. Throw profiles along the strike of (a) the Waitarere Fault and (b) the Okupe and Moana faults. Profiles are restricted to horizons H1 to H4 and H7 (see Figure 10 caption for details). Error bars on the H4 horizon are shown only for the Waitarere Fault, where measurements are interpolated. The horizon onlaps the basement west of the fault. Error bars on basement throw are indicated where interpretation of basement reflector is masked by reverberated energy and the resulting uncertainty is large (line CR31, Figure 10). The error bars indicate the extreme measurements, and the label is positioned at the best estimate of the throw at the location. (c) Cumulative throw profiles for the Waitarere, Okupe, and Moana faults. Individual profiles are decimated using a 1-km segment length before summation into the cumulative profiles.

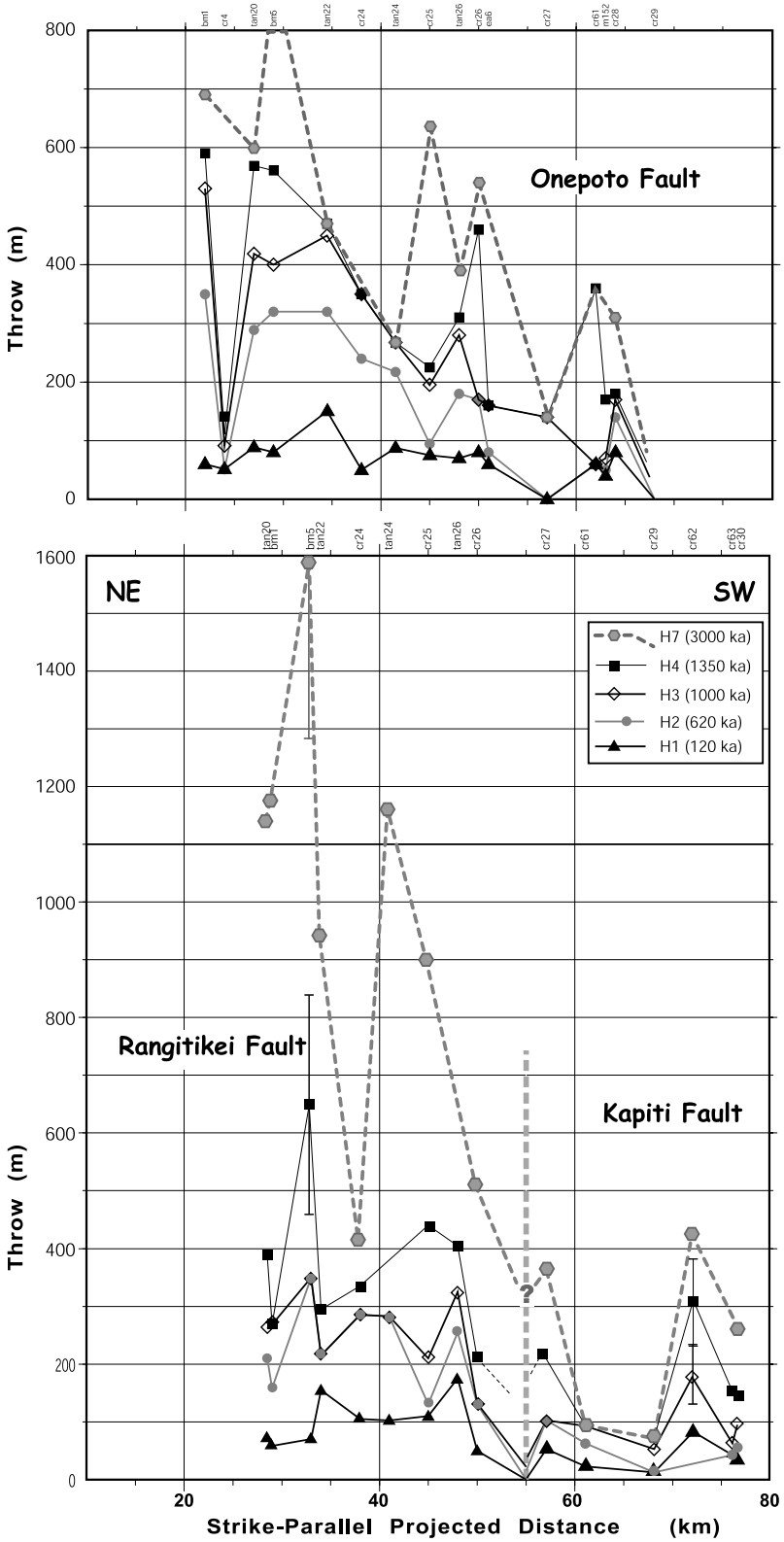

Figure 13. Throw profiles along the strike of the Onepoto, Rangitikei, and Kapiti faults. Profiles are restricted to horizons H1 to H4 and H7 (see Figure 11 caption for details). Thick gray dashed line indicates transition from the Rangitikei Fault to the Kapiti Fault.

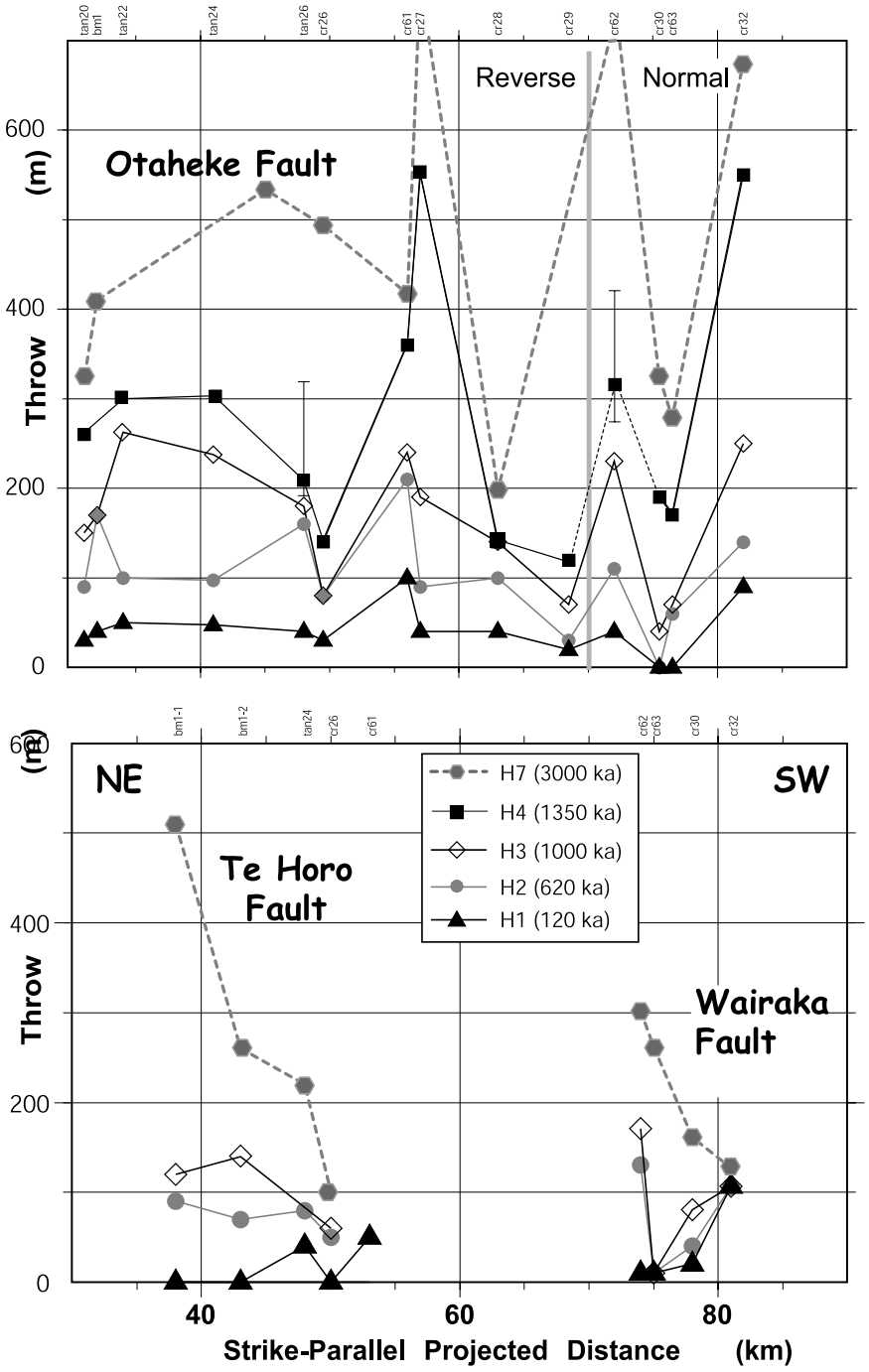

Figure 14. Throw profiles along the strike of the Otaheke, Te Horo, and Wairaka faults. The high uncertainties result from the poor seismic resolution (only horizons H1 to H4 are identified) and a lack of seismic profiles in the coastal zone. The thick vertical gray line indicates the transition from reverse to normal displacements along the Otaheke North and Otaheke South faults, respectively (see Figure 11 caption for details).

almost 5 mm yr^{-1} from 120 to 3 ka. *Nicol et al.* [2002, Table 2] indicate that displacement rates on the contractional Huangarua Fault increased from 0.4 to 0.5 mm yr^{-1} between 1600 and 60 ka to approximately 0.7 mm yr^{-1} from 60 to 12 ka. The highest time-averaged displacement rates of $\sim$1 mm yr^{-1}, however, were observed on the Huangarua Fault between 2000 and 1600 ka, when initiation of contraction is also likely to have occurred in the KMFS.

[62] Clearly, deformation across the plate boundary zone varies substantially in time and space. Nonetheless, there seems to be a consistency between different geo-

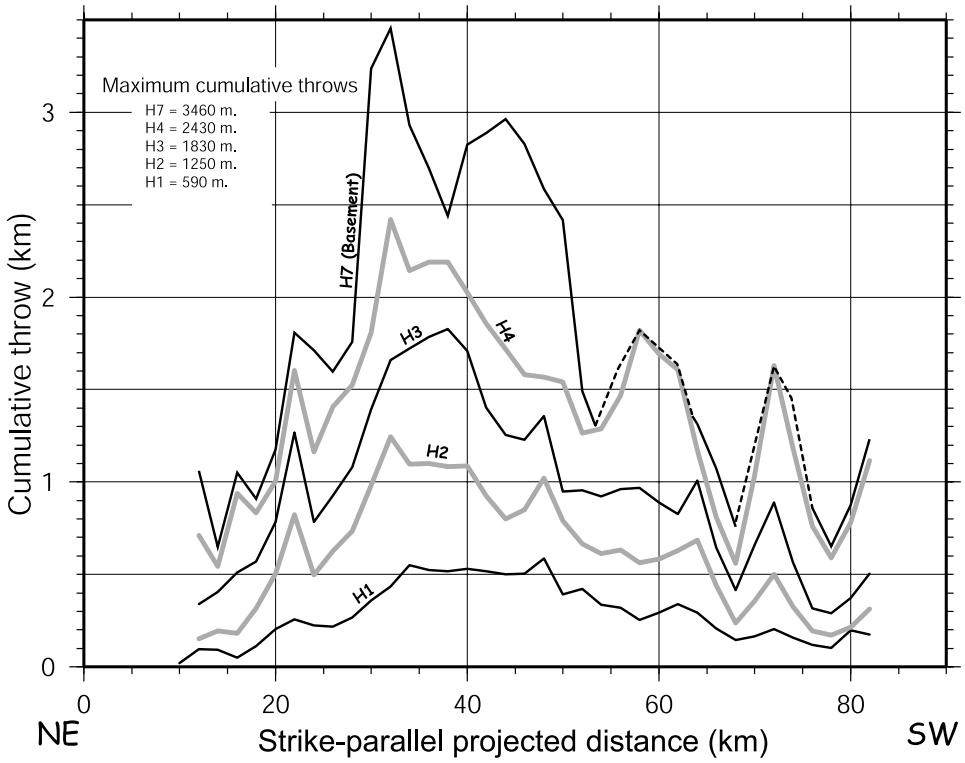

Figure 15. Cumulative throw profiles for the KMFS for horizons H1 to H4 and H7 (see Figure 11 caption for details). A 2-km decimation of individual throw profiles was undertaken before summation into cumulative profiles. Profile minima in the cumulated throw profiles may indicate segment boundaries within the linked KMFS fault array.

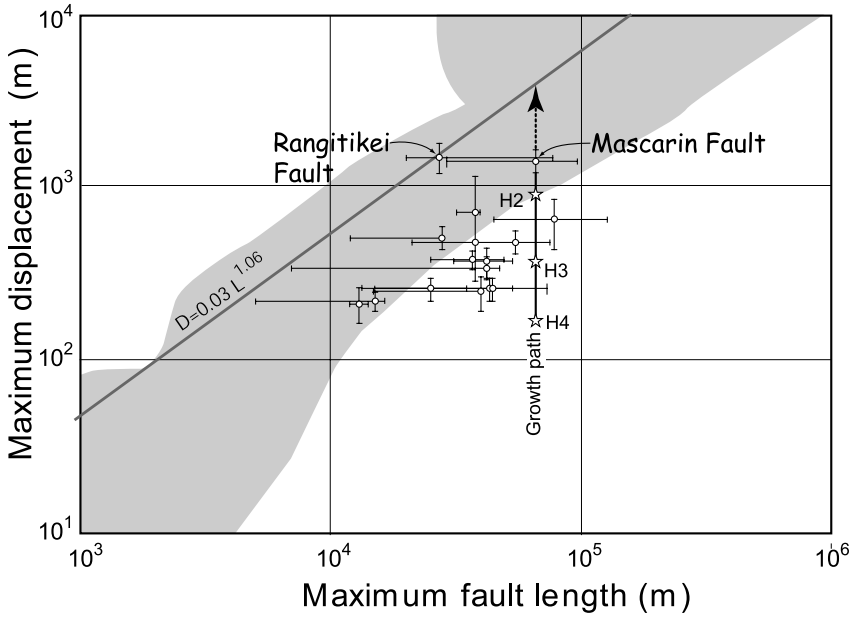

Figure 16. Log-log plot of maximum displacement versus length for faults in the KMFS. Circles indicate the best estimate of the H7 (3000 ka) throw (D)/length (L) relationship for faults in the KMFS with estimated error bars. H7 is assimilated to the basement horizon. The Mascarin Fault growth trend is indicated by the solid arrow, and the stars indicate the D/L positions at 1350, 1000, and 620 ka. The dashed arrow indicates the possible future growth path to achieve the best fit ($D = 0.03L^{1.06}$, thick gray line) with a global fault data set (shaded area) of *Schlische et al.* [1996].

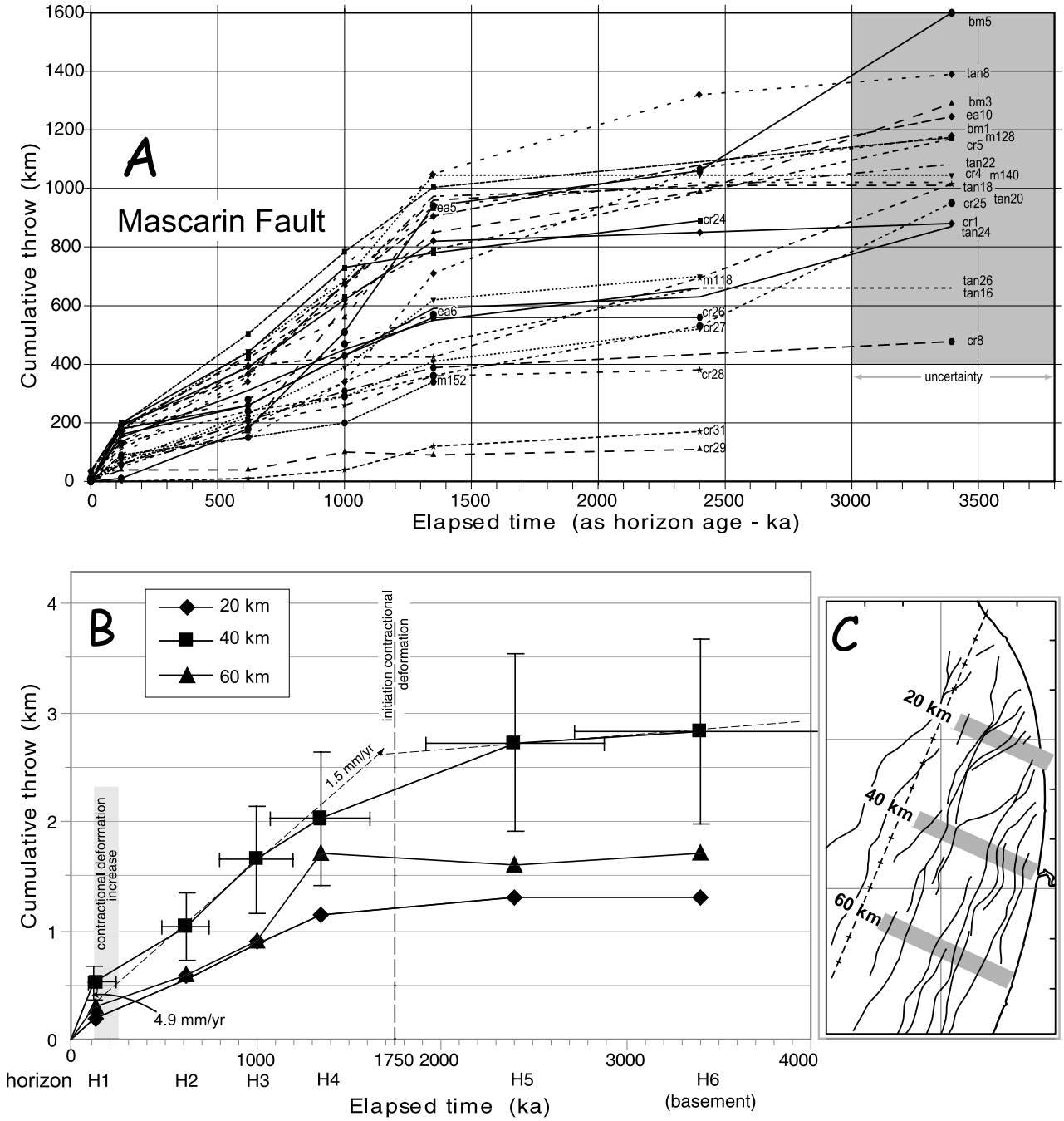

Figure 17. (a) Throw versus horizon ages for all piercing points (i.e., seismic profiles) along the Mascarin Fault. All piercing points are shown. (b) Average maximum throws versus Horizon ages along strike for all KMFS faults. Averaged maximum throws were calculated at 18–22, 38–42, and 58–62 km along strike. Relative errors of 30% are assigned to these values, as they represent the sum of the errors on ages and horizon offsets across faults (see text). (c) Location of across-strike profiles at 20, 40, and 60 km along the strike projection axis (Figure 5).

logical observations that suggests that a significant increase in contractional strain occurred across both the forearc and back arc of the southern Hikurangi subduction system at about 1750 ka and increased again at about 100 ka.

6.3.4. Regional Implications

[63] We calculate ~3460 m of cumulated vertical displacement of the basement horizon across the reverse faults of the KMFS (Figure 15), and a further ~200 m associated with reverse faulting between the coast and the foot of the

Table 3. Maximum Dip Slip Rates in the KMFS[a]

Fault	Dip	DS.H1	DS.H4	DS.H4-H1
Hokio	70	0.80 ± 0.24	0.19 ± 0.06	0.13 ± 0.04
Kapiti	70	0.71 ± 0.21	0.25 ± 0.07	0.20 ± 0.06
Mascarin	70	1.77 ± 0.53	0.83 ± 0.25	0.74 ± 0.22
Moana	70	0.65 ± 0.19	0.32 ± 0.09	0.28 ± 0.08
Okupe	70	0.53 ± 0.16	0.21 ± 0.06	0.18 ± 0.05
Onepoto	70	1.33 ± 0.4	0.47 ± 0.14	0.38 ± 0.11
Otaheke-Nth	70	0.89 ± 0.27	0.45 ± 0.13	0.41 ± 0.12
Otaheke-Sth	70	0.80 ± 0.24	0.43 ± 0.13	0.40 ± 0.12
Rangitikei	80	1.48 ± 0.44	0.49 ± 0.15	0.39 ± 0.12
Santoft	70	0.71 ± 0.21	0.26 ± 0.08	0.22 ± 0.06
Tangimoana	70	0.29 ± 0.09		
Te Horo	70	0.44 ± 0.13		
Wairaka-Nth	80	0.17 ± 0.05	0.20 ± 0.06	0.21 ± 0.06
Waitarere	70	0.63 ± 0.19	0.34 ± 0.1	0.31 ± 0.09

[a]Dip slip rates are calculated using a fault dip of 70° for all fault except for Rangitikei and Wairaka where a fault dip of 80° is used. The associated error of 30% takes into account a possible fault dip ranging 65–75°. DS.H1, dip slip over the last 120 kyr (H1) period; DS.H4, dip slip over the last 1350 kyr (H4) period; DS.H4-H1, dip slip for the 1350–120 kyr (H1) period.

Axial Ranges [*Aharoni*, 1991]. The resulting ~3700 m of vertical separation accounts for 50–74% of the 5000–7000 m of elevation difference between the top of the Axial Ranges and the basement floor of the SWB. We infer that the remaining 1300–2300 m of separation must have been accommodated by distributed deformation. Such deformation might include small structures not resolved by the MCS system, and in particular faulting below the resolution of the high-resolution seismic reflection data, folding not associated with fault drag and basin-scale sediment warping.

[64] Horizontal shortening west of the Axial Ranges is quantified using two independent methods (Tables 4a–c).

Table 4b. Method 3, L0/L1 Measured on MCS Profiles[a]

L0/L1	Tan26	Tan24	Tan20	Average	Rate, 10^{-15} s^{-1}
H3	1.7	1.7	1.1	1.5	**0.5**
BAS	4.5	3.7	5	4.4	**1.4**

[a]Method 3 is that strain and strain rates are estimated from initial (l_0) and final (l_1) bed lengths measured on depth-converted seismic profiles.

Assuming 60°–75° fault dips, shortening across the KMFS measured along the basement reflector is ~1.35 ± 0.35 km, which represents 5 to 15% of the 9–28 km of total shortening accumulated across the upper plate over the last 5 Myr [*Nicol and Beavan*, 2003]. This implies an average shortening rate across the upper plate of 0.8 ± 0.4 mm yr^{-1} between the Axial Ranges and the Taranaki Fault if we attribute a 50% error as the sum of error on velocities, horizon picking and ages. This shortening rate represents a minimum value as some contractional deformation may have occurred before 1750 ka.

[65] From the shortening estimates, we calculate long-term horizontal strain rates. Because the general orientation of the seismic profiles (N110°E) is subperpendicular to the trend of the KMFS, where contractional deformation dominates (i.e., assuming there is no or a negligible amount of strike-slip motion), these estimates are thought to be representative of the contractional strain and strain rates across the basin. Contractional strain rates for the period 0 to 3000 ka range from 0.5 to 1.4 × 10^{-15} s^{-1}, which compare well with 0.5–1 × 10^{-15} s^{-1} strain rates calculated using shortening along horizon H3 (1000 ka). A maximum strain rate of 2.3 × 10^{-15} s^{-1} is calculated using the age of 120 ka for H1 (Table 4).

[66] In the forearc, east of the Axial Ranges, long-term strain rates along a N150°E direction are 2.38 × 10^{-15} s^{-1}

Table 4a. Evaluation of Strain and Strain Rates West of the North Island Axial Ranges[a]

			Shortening (ΔL) (Percent Based on 25-km-Wide Zone)						Strain ε = D/(L.tanα) (L = 25 km) Strain Rate, 10^{-15} s^{-1}			
			α = 65°		α = 70°		α = 75°					
	Timing, ka	D Cumulative, m	Meters	Percent	Meters	Percent	Meters	Percent	65°	70°	75°	Average
Method 1[b]												
H1	120	590	275	1.1	215	0.9	158	0.6	2.9	2.3	1.7	2.3
H1	240	590	275	1.1	215	0.9	158	0.6	1.5	1.1	0.8	1.1
H2	620	1250	583	2.3	455	1.8	335	1.3	1.2	0.9	0.7	0.9
H3	1000	1830	853	3.4	666	2.7	490	2.0	1.1	0.8	0.6	0.8
H4	1350	2430	1133	4.5	884	3.5	651	2.6	1.1	0.8	0.6	0.8
Bast min	2400	3700	1725	6.9	1347	5.4	991	4.0	0.9	0.7	0.5	0.7
Bast max	3000	3700	1725	6.9	1347	5.4	991	4.0	0.7	0.6	0.4	0.6
Method 2[c]												
Min	3800	5000	2332	9.3	1820	7.3	1340	5.4	0.8	0.6	0.4	0.6
Max	3000	7000	3264	13.1	2548	10.2	1876	7.5	1.4	1.1	0.8	1.1

[a]Three independent methods were used to estimate strain and strain rates. Method 1 is a single fault proxy across a 25-km-wide deformed zone. For each horizon, we calculated shortening using ΔL = (L tan α) and strain rate ε = D/(L tan α) for three constant fault dips α (65, 70, and 75°), where L is a fault zone width of 25 km and D is cumulative throw across the KMFS for the given timing. The average strain is calculated. Method 2 is similar to method 1 but assumes that the 5–7 km elevation difference of the top of the basement between the top of the Axial Ranges to the basement reflector at the bottom of the SWB was acquired between 3000 ka (H7) and 2600 ka (H6). The average strain is calculated.

[b]Cumulative throw is measured on MCS profiles.

[c]There is 5–7 km vertical separation of the top basement from top axial ranges to SWB depot center.

Table 4c. Published Strain Rates in the Forearc Domain Derived From Geological and Geodetic Data

Periods	Regional Shortening Strain Rates, 10^{-15} s^{-1}	Source
0–100 ka	9.8 ± 2.9	*Lamb and Vella* [1987]
0–2000 ka	2.38 ± 0.4	*Nicol et al.* [2002]
0–1930 A.D.	19 ± ?	*Walcott* [1978] (geodetic)

since 1600–2000 ka [*Nicol et al.*, 2002] and 9.8 × 10^{-15} s^{-1} for the last 100 kyr [*Lamb and Vella*, 1987]. The latter value is 4 times larger than that calculated for the 0–120 ka period across the KMFS using an age of 120 ka for H1 and 1 order of magnitude larger when using the alternative (older) age of 240 ka for H1. Strain rates calculated for the periods 0–3000 and 0–1000 ka west of the Axial Ranges are ~2–5 times smaller than that calculated in the forearc basin for the same periods, which shows a sharp attenuation of strain across the NIDFB and Axial Ranges. Long-term (2–5 Myr) strain rates derived from geological data provide information on permanent deformation associated with the plate boundary, while short-term (5–10 years) strain rates relate to interseismic strain accumulation [*Holt and Haines*, 1995; *Walcott*, 1984]. These authors suggested that short-term strain rates derived from geodetic data were comparable to the average long-term deformation. In our case, long-term strain rates across the KMFS for the last 120 kyr and 0–3000 kyr are 8–17 times smaller than geodetic strain rates across the axial ranges at the latitude of the SWB (19 × 10^{-15} s^{-1} [*Walcott*, 1978]).

[67] The KMFS is located midway between the Taranaki Fault and the NIDFB, to the west and east, respectively, of the SWB (Figure 18). To the east, more than 4 km of vertical displacement has occurred across the NIDFB, mainly by deformation on the Wellington-Wairarapa faults at the same latitude as the KMFS [*Beanland et al.*, 1998], during the last phase of contractional deformation, i.e., concomitant with deformation along the KMFS. To the west, more than 5 km of vertical displacement has occurred across the Taranaki Fault essentially during the Miocene [*Nicol et al.*, 2004], but may have persisted until at least 2600 ka [*Proust et al.*, 2005]. The initiation of contractional deformation along the eastern edge of the SWB at 1750 ka [this study] suggests a transfer of strain from the Taranaki Fault to the eastern flank of the SWB may have occurred during the quiescent period of faulting within the KMFS between 2600 and 1750 ka.

[68] The Mascarin and Rangitikei faults account for approximately 80% of the displacement accommodated across the KMFS. Although we have no direct indication of the depths to which the Mascarin and Rangitikei faults extend, there is indirect evidence that suggests these faults could reach the plate interface at ~40 km beneath the SWB. In particular, the continuous occurrence of earthquakes to a depth of 40 km was interpreted by *Stern et al.* [1992] to be indicative of the absence of a brittle-ductile transition zone beneath the SWB, implying that upper crustal faults could propagate to such depths. Assuming that the fault heights are approximately half their lengths [*Nicol et al.*, 2002], the 95 km maximum length of the Mascarin Fault and its steep dip are consistent with an inferred linkage to the plate interface. The uplift and tilt of the basement block between the SWB and the forearc basin are clearly controlled by the KMFS and NIDFB (Figure 18). This is consistent with linkage of the KMFS with the plate interface.

7. Conclusions

[69] The KMFS is a major contractional fault system that is associated with the regional tectonic deformation of the upper plate in the Pacific-Australia plate boundary deformation zone in the central New Zealand region. The KMFS is distinctive in that it is located in a region where high subsidence and sedimentation rates (>1 mm yr^{-1}) occur in a compressive setting. Perhaps uniquely for such contractional tectonic environments, good preservation of time horizons in both hanging walls and footwalls provide excellent controls, both in space and time, on the evolution of the reverse fault population within the KMFS. This study provides detailed qualitative and quantitative information on the evolution of the deformation west of the Axial Ranges of the North Island. In particular, the study provides estimates of fault lengths and dip-slip rates on individual faults in the KMFS, as well as strain and strain rates across the fault system as a whole. Furthermore, the study addresses the implications of such fault behavior for both general models of fault

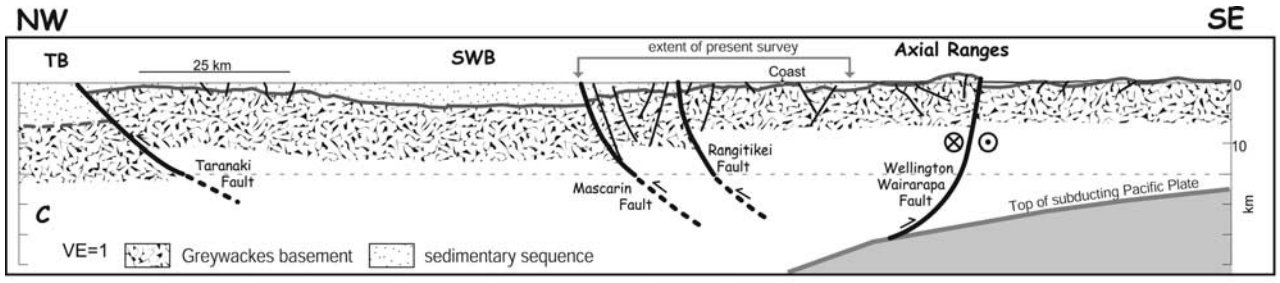

Figure 18. Synthetic regional crustal cross section compiled from cross sections from *Aharoni* [1991], *Anderton* [1981], and *Katz and Leask* [1990].

growth and for the regional tectonics of the plate boundary in central New Zealand by providing further constraints on the strain budget for the upper plate.

[70] Reverse faults in the KMFS originated from inversion of preexisting normal basement faults. Fault locations have remained fixed with no lateral fault propagation since 1750 ka and in many cases for at least the last 2600 kyr. Maximum dip-slip rates on individual faults are 1.77 ± 0.5 mm yr^{-1} for the 0–120 ka period and 0.74 ± 0.23 mm yr^{-1} for the 120–1350 ka period. Variations in the maximum long-term cumulative slip rates observed across the entire KMFS indicate three successive periods of compressive tectonics: (1) 3000–1750 ka, which was a relatively quiescent period with throw rates less than 1 mm yr^{-1}; (2) 1750–120 ka when throw rates were rapid ($\sim$2 mm yr^{-1}); and (3) 120–0 ka during which throw rates increased sharply, reaching maximum values of $\sim$5 mm yr^{-1}. There is a marked decrease in contractional strain rates west of the Axial Ranges, compared with that in the forearc basin to the east.

[71] Scaling relations and the lateral evolution of individual faults suggest that the KMFS represents a coherent, reverse fault system that has developed by mechanisms comparable to the coherent fault model defined for normal fault arrays [*Walsh et al.*, 2002]. This observation indicates that KMFS faults are kinematically dependent. The fault system developed in a low contractional strain setting, with interactions between faults resulting in the conservation of strain along the fault system. Strike-parallel throw profiles for individual faults and cumulative throw estimates across the entire KMFS are symmetrical about the point of maximum displacement (bell-shaped). Individual faults acquired their length early in the history of the fault system and follow a constant fault length model similar to that of *Walsh et al.* [2002].

[72] The possible link of the main structures within the KMFS with the subduction interface has direct consequences for the seismic hazard related to large subduction earthquakes in the region [*Reyners*, 1998], and there is a need to reassess this hazard in southern North Island in light of this work. This study also has the potential to assess the extent of coupling over geological periods of time along the subduction interface and along large reverse and strike-slip faults in the upper plate.

[73] **Acknowledgments.** We used Globe Claritas® seismic processing software of the Institute of Geological and Nuclear Sciences (Lower Hutt, New Zealand) to process NIWA MCS data. We thank Miles Dunkin (NIWA) for digitizing all structural interpretations and Erika McKay (NIWA) for drafting the figures. Mike Stevens (NIWA) processed part of the MCS data, and early comments from Andy Nicol (GNS) greatly helped in improving an earlier version of this manuscript. Reviews from Jarg Pettinga (Canterbury University) and Daniel Koehn were instrumental in completing this manuscript. Yearly travel between France and New Zealand was funded by the French Ministry of Foreign Affairs in the framework of the France and New Zealand Cultural Agreement of 1977 and was extremely beneficial to the project at all stages. We acknowledge the financial support of FRST contract C01X0203 and INSU-CNRS "Intérieur de la Terre" program.

References

Aharoni, E. (1991), Seismic reflection study across the Horowhenua coastal plain, North Island, New Zealand, M.Sc. thesis, 169 pp., Victoria Univ. of Wellington, Wellington.

Anderton, P. W. (1981), Structure and evolution of the South Wanganui Basin, New Zealand, *N. Z. J. Geol. Geophys.*, *24*, 39–63.

Barnes, P. M., B. Mercier de Lépinay, J.-Y. Collot, J. Delteil, and J.-C. Audru (1998), Strain partitioning in the transition area between oblique subduction and continental collision, Hikurangi margin, New Zealand, *Tectonics*, *17*(4), 534–557.

Barnes, P. M., A. Nicol, and T. Harrison (2002), Late Cenozoic evolution and earthquake potential of an active listric thrust complex above the Hikurangi subduction zone, New Zealand, *Geol. Soc. Am. Bull.*, *114*(11), 1379–1405.

Beanland, S. (1995), The North Island dextral fault belt, Hikurangi subduction margin, New Zealand, Ph.D. thesis, 341 pp., Victoria Univ. of Wellington, Wellington.

Beanland, S., A. Melhuish, A. Nicol, and J. M. Ravens (1998), Structure and deformational history of the inner forearc region, Hikurangi subduction margin, New Zealand, *N. Z. J. Geol. Geophys.*, *41*, 325–342.

Carter, R. M., and T. R. Naish (1998), A review of Wanganui Basin, New Zealand: Global reference section for shallow marine, Plio-Pleistocene (2.5–0 Ma) cyclostratigraphy, *Sediment. Geol.*, *122*, 37–52.

Cartwright, J. A., B. Trudgill, and C. Mansfield (1995), Faults growth by segment linkage: An explanation for scatter in maximum displacement and trace length data from the Canyonlands grabens of S. E. Utah, *J. Struct. Geol.*, *17*, 1319–1326.

Chapman, T. J., and A. W. Meneilly (1991), The displacement patterns associated with a reverse-reactivated, normal growth fault, in *The Geometry of Normal Faults*, edited by A. M. Roberts, G. Yielding, and B. Friedman, *Geol. Soc. Spec. Publ.*, *56*, 183–191.

Childs, C., S. J. Easton, B. C. Vendeville, M. P. A. Jackson, S. T. Lin, J. J. Walsh, and J. Waterson (1993), Kinematic analysis of faults in a physical model of growth faulting above a viscous salt analogue, *Tectonophysics*, *228*, 313–329.

Childs, C., A. Nicol, J. J. Walsh, and J. Watterson (2003), The growth and propagation of synsedimentary faults, *J. Struct. Geol.*, *25*, 633–648.

Collot, J.-Y., et al. (1996), From oblique subduction to intra-continental transpression: Structures of the southern Kermadec-Hikurangi margin from multibeam bathymetry, side scan sonar and seismic reflection, *Mar. Geophys. Res.*, *18*, 357–381.

Cowie, P. A., and G. P. Roberts (2001), Constraining slip rates and spacings for active normal faults, *J. Struct. Geol.*, *23*, 1901–1915.

Cowie, P. A., and C. H. Scholz (1992), Displacement-length scaling relationship for faults: Data synthesis and discussion, *J. Struct. Geol.*, *14*, 1149–1156.

Darby, D., and J. Beavan (2001), Evidence from GPS measurements for contemporary interplate coupling on the southern Hikurangi subduction thrust and for partitioning of strain in the upper plate, *J. Geophys. Res.*, *106*(B12), 30,881–30,891.

DeMets, C., R. G. Gordon, D. F. Argus, and S. Stein (1994), Effect of recent revisions to the geomagnetic reversal time scale on estimates of current plate motions, *Geophys. Res. Lett.*, *21*(20), 2191–2194.

Fleming, C. A. (1953), The geology of Wanganui subdivision: Waverley and Wanganui sheet districts (N137 and N138), *N. Z. Geol. Surv. Bull.*, *52*, 1–362.

Garrick, R. A., and S. J. Gibowicz (1983), Continuous swarm-like seismicity: The Wanganui, New Zealand, earthquakes, *Geophys. J. R. Astron. Soc.*, *75*, 493–512.

Ghani, M. A. (1978), Late Cenozoic vertical movements in the southern North Island, New Zealand, *N. Z. J. Geol. Geophys.*, *21*, 117–125.

Harding, T. P. (1990), Identification of wrench faulting using subsurface data: Criteria and pitfalls, *AAPG Bull.*, *74*(10), 1590–1609.

Hayward, A. B., and R. H. Graham (1989), Some geometrical characteristics of inversion, in *Inversion Tectonics*, edited by M. A. Cooper and D. G. Williams, *Geol. Soc. Spec. Publ.*, *44*, 153–175.

Holt, W. E., and A. J. Haines (1995), The kinematics of northern South Island, New Zealand, determined from geologic strain rates, *J. Geophys. Res.*, *100*(B9), 17,991–18,010.

Hunt, T. M. (1980), Basement structure of the Wanganui Basin, onshore, interpreted from gravity data, *N. Z. J. Geol. Geophys.*, *23*, 1–16.

Jackson, J., R. J. Van Dissen, and K. R. Berryman (1998), Tilting of active folds and faults in the Manawatu region, New Zealand: Evidence from surface drainage patterns, *N. Z. J. Geol. Geophys.*, *41*, 377–385.

Kamp, P. J. J. (1986), Late Cretaceous-Cenozoic tectonic development of the southwest Pacific region, *Tectonophysics*, *121*, 225–251.

Kamp, P. J. J., and G. M. Turner (1990), Pleistocene unconformity-bounded shelf sequences (Wanganui Basin, New Zealand) correlated with global isotope record, *Sediment. Geol.*, *68*, 155–161.

Kamp, P. J. J., A. J. Vonk, K. J. Bland, R. Funnell, A. G. Griffin, S. Hayton, A. J. W. Hendy, A. P. McIntyre, C. S. Nelson, and T. Naish (2002), Megasequence architecture of the Taranaki, Wanganui, and King Country basins and Neogene progradation

of two continental margin wedges across western New Zealand, paper presented at 2002 New Zealand Petroleum Conference, Minist. of Commer., Wellington.

Katz, R., and B. Leask (1990), The South Wanganui Basin—A neglected hydrocarbon prospect, *Pet. Explor. N. Z. News*, *25*, 19–25.

Lamb, S. H., and P. Vella (1987), The last million years of deformation in part of the New Zealand plate-boundary zone, *J. Struct. Geol.*, *9*, 877–891.

Lewis, K. B., and J. R. Pettinga (1993), The emerging, imbricate frontal wedge of the Hikurangi margin, in *Sedimentary Basins of the World*, vol. 2, *South Pacific Sedimentary Basin*, edited by P. F. Ballance, pp. 225–250, Elsevier, New York.

Mansfield, C. S., and J. A. Cartwright (1996), High resolution fault displacement mapping from three-dimensional seismic data: Evidence for dip linkage during fault growth, *J. Struct. Geol.*, *18*, 249–263.

Melhuish, A., R. J. Van Dissen, and K. R. Berryman (1996), Mount Stewart–Halcombe Anticline: A look inside a growing fold in the Manawatu region, New Zealand, *N. Z. J. Geol. Geophys.*, *39*, 123–133.

Meyer, V., A. Nicol, C. Childs, J. J. Walsh, and J. Watterson (2002), Progressive localisation of strain during the evolution of a normal fault population, *J. Struct. Geol.*, *24*, 1215–1231.

Moore, P. R., and D. A. Francis (1988), Geology of Kapiti Island, central New Zealand, report, 23 pp., N. Z. Geol. Surv., Lower Hutt, New Zealand.

Naish, T. R., R. M. Carter, and B. J. Pillans (1999), High resolution chronology for the Plio-Pleistocene, Wanganui Basin, New Zealand, in *The High Resolution Chronostratigraphic and Sequence Stratigraphic Record of the Plio-Pleistocene, Wanganui Basin, New Zealand*, edited by R. M. Carter and T. R. Naish, *Folio Ser. 2*, poster 2, version 1999.1, Inst. of Geol. and Nucl. Sci., Lower Hutt, New Zealand.

Nicol, A., and J. Beavan (2003), Shortening of an overriding plate and its implication for slip on a subduction thrust, central Hikurangi margin, New Zealand, *Tectonics*, *22*(6), 1070, doi:10.1029/2003TC001521.

Nicol, A., R. J. Van Dissen, P. Vella, B. Alloway, and A. Melhuish (2002), Growth of contractional structures during the last 10 m.y. at the southern end of the emergent Hikurangi forearc basin, New Zealand, *N. Z. J. Geol. Geophys.*, *45*, 365–385.

Nicol, A., V. Stagpoole, and G. Maslen (2004), Structure and petroleum potential of the Taranaki fault play, paper presented at 2004 New Zealand Petroleum Conference, Minist. of Commer., Wellington.

Nielsen, S. B., and U. Bayer (2003), Dynamics of sedimentary basin inversion: Observations and modelling, *Tectonophysics*, *373*, 1–3.

Pillans, B. (1986), A late Quaternary uplift map from North Island, New Zealand, *Bull. R. Soc. N. Z.*, *24*, 409–417.

Pillans, B. (1990), Vertical displacement rates on Quaternary faults, Wanganui Basin, *N. Z. J. Geol. Geophys.*, *33*, 271–275.

Pillans, B. (1991), New Zealand Quaternary stratigraphy: An overview, *Quat. Sci. Rev.*, *10*, 405–418.

Proust, J.-N., G. Lamarche, and S. Nodder (2005), Sedimentary architecture of a Plio-Pleistocene proto back-arc basin, Wanganui Basin, New Zealand. Sedimentary Geology, *Sediment. Geol.*, in press.

Reyners, M. (1998), Plate coupling and the hazard of large subduction thrust earthquakes at the Hikurangi subduction zone, New Zealand, *N. Z. J. Geol. Geophys.*, *41*, 343–354.

Robinson, R. (1986), Seismicity, structure and tectonics of the Wellington region, New Zealand, *Geophys. J. R. Astron. Soc.*, *87*, 379–409.

Schlische, R. W., S. S. Young, R. V. Ackermann, and A. Gupta (1996), Geometry and scaling relations of a population of very small rift-related normal faults, *Geology*, *24*(8), 683–686.

Sibson, R. H. (1995), Selective fault reactivation during basin inversion: Potential for fluid redistribution through fault-valve action, in *Basin Inversion*, edited by J. G. Buchanan and P. G. Buchanan, *Geol. Soc. Spec. Publ.*, *88*, 3–19.

Spörli, K. B. (1980), New Zealand and oblique-slip margins: Tectonic development up to and during the Cainozoic, *Spec. Publ. Int. Assoc. Sedimentol.*, *4*, 147–170.

Stern, T. A., and F. J. Davey (1989), Crustal structure and origin of basins formed behind the Hikurangi subduction zone, New Zealand, in *Origin and Evolution of Sedimentary Basins and Their Energy and Mineral Resources*, *Geophys. Monogr. Ser.*, vol. 48, edited by R. A. Price, pp. 73–86, AGU, Washington, D. C.

Stern, T. A., G. M. Quinlan, and W. E. Holt (1992), Basin formation behind an active subduction zone: Three-dimensional flexural modelling of Wanganui Basin, New Zealand, *Basin Res.*, *4*, 197–214.

Stern, T. A., G. M. Quinlan, and W. E. Holt (1993), Crustal dynamics associated with the formation of Wanganui Basin, New Zealand, in *Sedimentary Basins of the World,* vol. 2, *South Pacific Sedimentary Basins*, edited by P. F. Ballance, pp. 213–223, Elsevier, New York.

Stirling, M. W., G. McVerry, K. R. Berryman, P. McGinty, P. Villamor, R. J. Van Dissen, D. Dowrick, J. Cousins, and R. Sutherland (2000), Probabilistic seismic hazard assessment of New Zealand: New active fault data, seismicity data, attenuation, relationships and methods, report, 117 pp., Inst. of Geol. and Nucl. Sci., Lower Hutt, New Zealand.

Thompson, T. L., W. L. Leask, and B. T. May (1994), Petroleum potential of the South Wanganui Basin, in *1994 New Zealand Petroleum Conference Proceedings: The Post Maui Challenge—Investment and Development Opportunities*, pp. 108–127, Minist. of Commer., Wellington.

Thore, P., A. Shtuka, M. Lecour, T. Ait-Ettajer, and R. Cognot (2002), Structural uncertainties: Determination, management, and applications, *Geophysics*, *67*(3), 840–852.

Van Dissen, R. J., and K. R. Berryman (1996), Surface rupture earthquakes over the last ~ 1000 years in the Wellington region, New Zealand, and implications for ground shaking hazard, *J. Geophys. Res.*, *101*(B3), 5999–6019.

Walcott, R. I. (1978), Geodetic strains and large earthquakes in the axial tectonic belt of North Island, New Zealand, *J. Geophys. Res.*, *83*, 4419–4429.

Walcott, R. I. (1984), The kinematics of the plate boundary zone through New Zealand, a comparison of short and long term deformation, *Geophys. J. R. Astron. Soc.*, *79*, 613–633.

Walsh, J. J., J. Watterson, C. Childs, and A. Nicol (1996), Ductile strain effects in the analysis of seismic interpretations of normal fault systems, in *Modern Developments in Structural Interpretation, Validation and Modelling*, edited by P. G. Buchanan and D. A. Niewland, *Geol. Soc. Spec. Publ.*, *99*, 27–40.

Walsh, J. J., A. Nicol, and C. Childs (2002), An alternative model for the growth of faults, *J. Struct. Geol.*, *24*, 1669–1675.

Walsh, J. J., W. R. Bailey, C. Childs, A. Nicol, and C. G. Bonson (2003), Formation of segmented normal faults: A 3-D perspective, *J. Struct. Geol.*, *25*, 1251–1262.

Wilcox, R. E., T. P. Harding, and D. R. Seely (1973), Basic wrench tectonics, *Am. Assoc. Pet. Geol. Bull.*, *57*(1), 74–96.

Wilson, G. S., and D. M. McGuire (1995), Distributed deformation due to coupling across a subduction thrust: Mechanism of young tectonic rotation within the South Wanganui Basin, New Zealand, *Geology*, *23*(7), 645–648.

G. Lamarche and S. D. Nodder, National Institute of Water and Atmospheric Research (NIWA) Ltd., Private Bag 14-901, Wellington, New Zealand. (g.lamarche@niwa.co.nz)

J.-N. Proust, Géosciences Rennes, Université de Rennes 1, Campus de Beaulieu, F-35042 Rennes cedex, France.

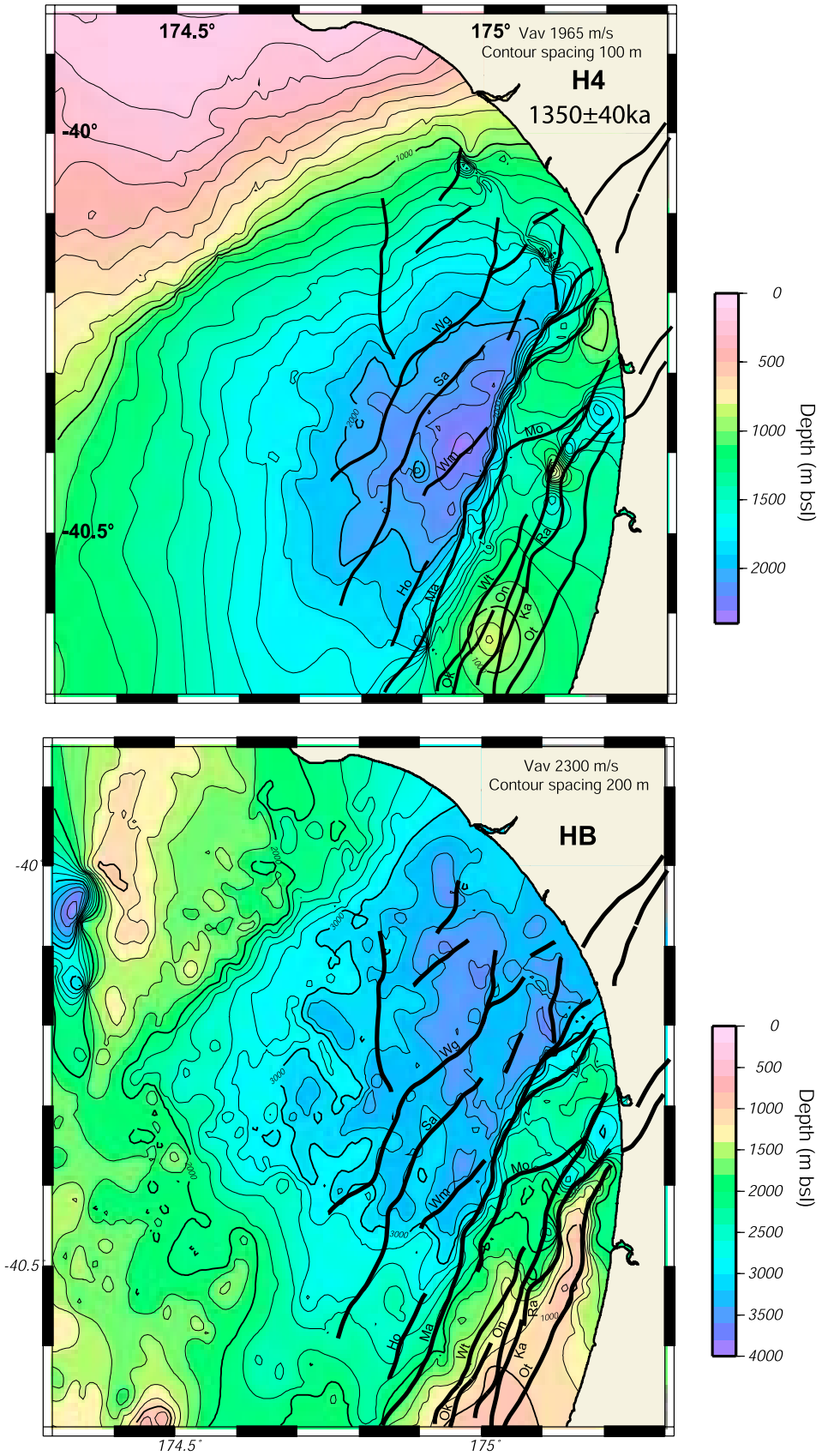
174.5°
175°
Vav 1965 m/s
Contour spacing 100 m
H4
1350±40ka
-40°
-40.5°
Wg
Sa
Mo
Wm
Ha
Ho
Ma
Wi
Or
Ka
Ot
Ra
0
500
1000
1500
2000
Depth (m bsl)
Vav 2300 m/s
Contour spacing 200 m
HB
-40°
-40.5°
174.5°
175°
Le
Sal
2500
3000
3500
4000

Figure 6

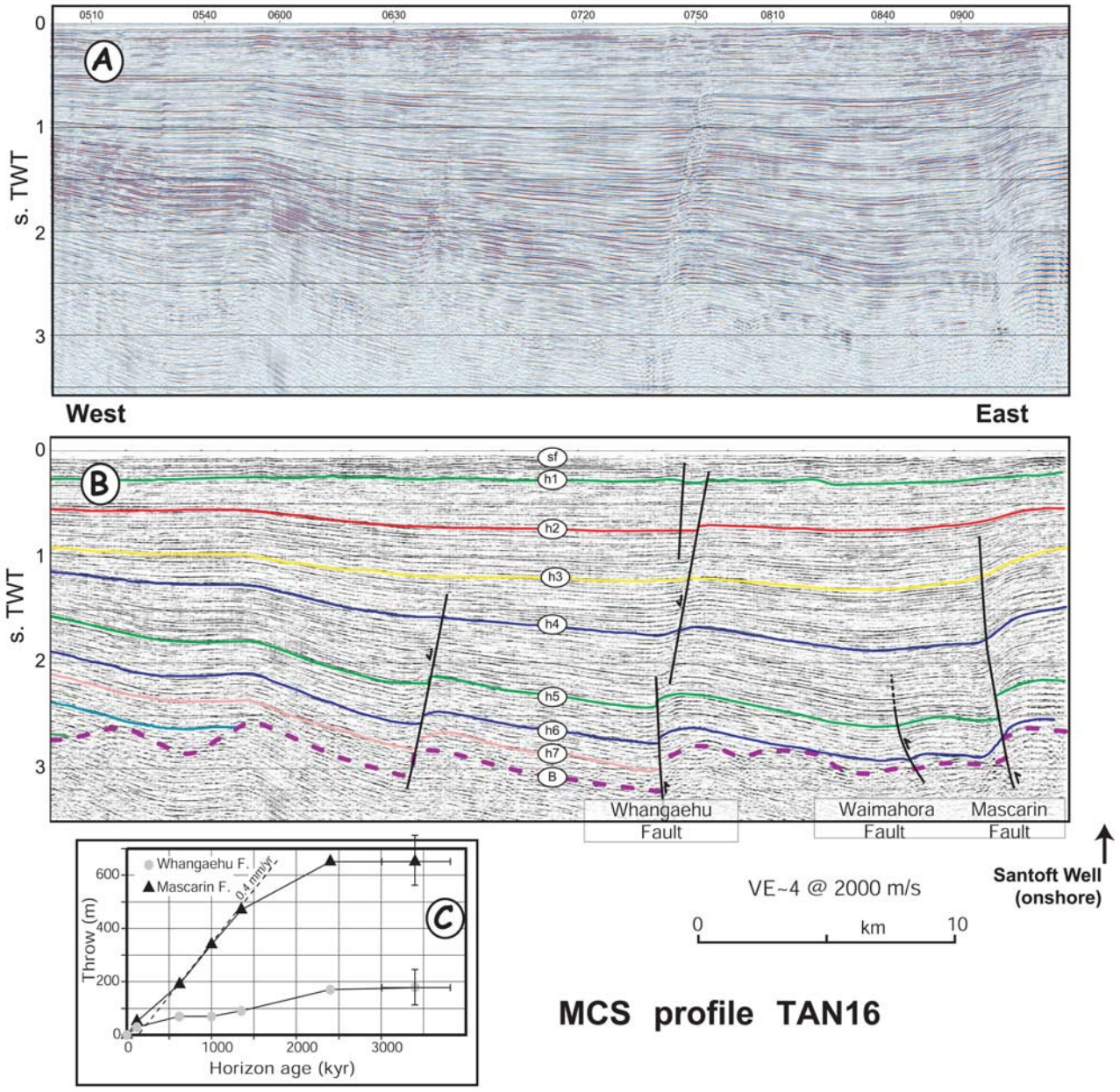

Figure 7. MCS profile TAN16 across the northern part of the KMFS. (a) Uninterpreted data. (b) Interpretation of seven key sedimentary horizons (h1–h7), seafloor (sf), and basement (B). Profile location is shown on Figures 4 and 5. (c) Time (age horizon ages) versus throw profiles for the Mascarin and Whangaehu faults. The Whangaehu Fault is located in the central part of the SWB; hence it is not part of the KMFS and was not used in subsequent calculations of cumulative throws and rates. Fault names are indicated at bottom of the interpreted profile.

Figure 6. Isodepth maps for horizon H4 (1350 ka) and the basement reflector (HB) as identified from interpretation of MCS data. Two-way travel times to each horizon were converted to depth using the average velocities indicated in the top right corner of each plot. Average velocities (Vav) were compiled as the weighted average of interval velocities calculated from stacking velocities picked during processing of industry and NIWA TAN MCS data. Stacking velocities from the CR survey are discarded as unreliable. The relative errors on depth are similar to that of velocities (30%) as the error on picking time is considered negligible. Faults interpreted in this study (Figure 5) are superimposed on each map and designated by the following abbreviations: Wg, Whangaehu; Sa, Santoft; Wm, Waimahora; Ho, Hokio; Ma, Mascarin; Mo, Moana; Wt, Waitarere; On, Onepoto; Ok, Okupe; Ra, Rangitikei; Ka, Kapiti; Ot, Otaheke.

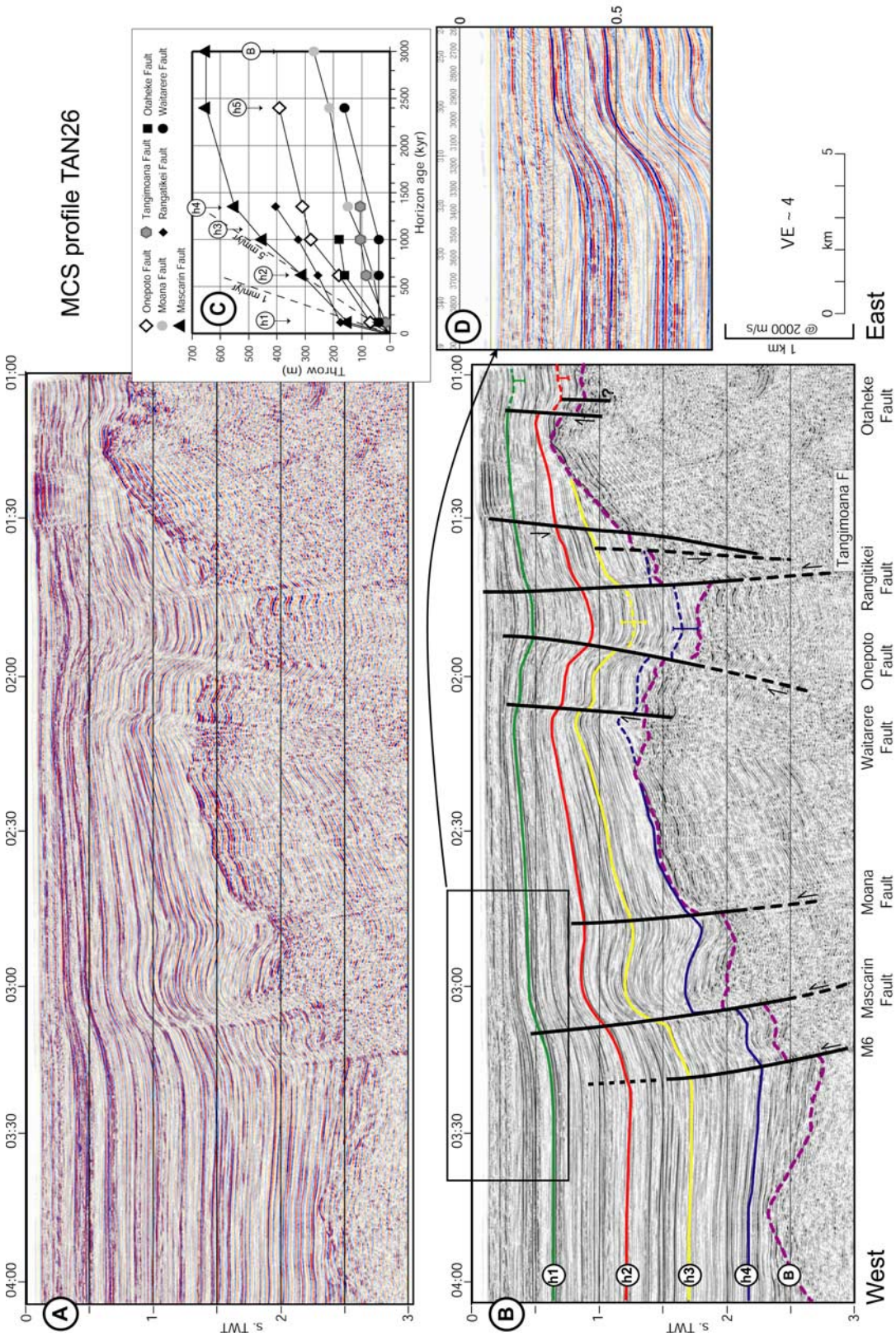
MCS profile TAN26
A
B
C
D
Onepoto Fault
Moana Fault
Mascarin Fault
Tangimoana Fault
Rangatikei Fault
Otaheke Fault
Waitarere Fault
Throw (m)
Horizon age (kyr)
5 mm/yr
1 mm/yr
h1
h2
h3
h4
h5
B
s. TWT
VE ~ 4
km
1 km
@ 2000 m/s
West
East
M6
Mascarin Fault
Moana Fault
Waitarere Fault
Onepoto Fault
Tangimoana F
Rangitikei Fault
Otaheke Fault

Figure 9

Figure 9. MCS profile TAN26 across the central part of the KMFS. (a) Uninterpreted data. (b) Interpretation of four key sedimentary horizons (h1–h4) and basement reflector (B). The southward rising of the graywacke basement results in the progressive thinning of the sedimentary sequence south of the depocenter (Figure 6) and the disappearance of key horizons older than H4. The colored error bars reflect the large uncertainty in the positions of the key horizons, associated with the lack of N-S oriented tie lines between the Onepoto and Rangitikei faults, as well as west of the Otaheke Fault. The question mark indicates uncertainty as to whether the subvertical fault in the footwall of the Otaheke Fault is reverse or normal. (c) Time (as horizon ages) versus throw. (d) Enlargement of near-surface layers showing fault growth and onlap features in the footwall of the Mascarin Fault indicating faulting activity post-H1 (120 ka) horizon. Note also the westward progradation of sediment. Profile location is shown on Figures 4 and 5. Fault names are indicated at bottom of the interpreted profile.